

Southern African summer-rainfall variability, and its teleconnections, on interannual to interdecadal timescales in CMIP5 models

Dieppois, B, Pohl, B, Cretat, J, Eden, JM, Sidibe, M, New, M, Rouault, M & Lawler, D

Author post-print (accepted) deposited by Coventry University's Repository

Original citation & hyperlink:

Dieppois, B, Pohl, B, Cretat, J, Eden, JM, Sidibe, M, New, M, Rouault, M & Lawler, D 2019, 'Southern African summer-rainfall variability, and its teleconnections, on interannual to interdecadal timescales in CMIP5 models' *Climate Dynamics*, vol. 53, no. 5-6, pp. 3505-3527. <https://dx.doi.org/10.1007/s00382-019-04720-5>

DOI 10.1007/s00382-019-04720-5

ISSN 0930-7575

ESSN 1432-0894

Publisher: Springer

The final publication is available at Springer via <http://dx.doi.org/10.1007/s00382-019-04720-5>

Copyright © and Moral Rights are retained by the author(s) and/ or other copyright owners. A copy can be downloaded for personal non-commercial research or study, without prior permission or charge. This item cannot be reproduced or quoted extensively from without first obtaining permission in writing from the copyright holder(s). The content must not be changed in any way or sold commercially in any format or medium without the formal permission of the copyright holders.

This document is the author's post-print version, incorporating any revisions agreed during the peer-review process. Some differences between the published version and this version may remain and you are advised to consult the published version if you wish to cite from it.

[Click here to view linked References](#)

1 **Southern African summer-rainfall variability, and its teleconnections, on**
2 **interannual to interdecadal timescales in CMIP5 models**

3
4 Bastien Dieppois ^{1,2,3}, Benjamin Pohl ⁴, Julien Crétat ^{4,5}, Jonathan Eden ¹, Moussa Sidibe ¹,
5 Mark New ⁶, Mathieu Rouault ^{2,7}, Damian Lawler¹

6
7 ¹ Centre for Agroecology, Water and Resilience, Coventry University, Coventry, UK

8 ² Department of Oceanography, MARE Institute, University of Cape Town, Cape Town, RSA

9 ³ School of Geography, Earth and Environmental Sciences, University of Birmingham,
10 Birmingham, UK

11 ⁴ Centre de Recherches de Climatologie, UMR 6282 Biogéosciences, CNRS/Université de
12 Bourgogne Franche Comté, Dijon, France

13 ⁵ IPSL/Laboratoire des Sciences du Climat et de l'Environnement, CEA-CNRS-UVSQ,
14 Université Paris Saclay, Gif-sur-Yvette, France

15 ⁶ African Climate & Development Initiative, University of Cape Town, Cape Town, RSA

16 ⁷ Nansen-Tutu Center for Marine Environmental Research, University of Cape Town, Cape
17 Town, RSA

18

19

20 Correspondence to: Bastien Dieppois, Centre for Agroecology, Water and Resilience

21 (CAWR), Coventry University, Ryton Gardens, Ryton on Dunsmore, Coventry, CV8 3LG,

22 UK. E-mail: bastien.dieppois@coventry.ac.uk

23

24

25

26 **Abstract** This study provides the first assessment of CMIP5 model performances in
27 simulating southern Africa (SA) rainfall variability in austral summer (Nov–Feb), and its
28 teleconnections with large-scale climate variability at different timescales. Observed SA
29 rainfall varies at three major timescales: interannual (2–8 years), quasi-decadal (8–13 years;
30 QDV) and interdecadal (15–28 years; IDV). These rainfall fluctuations are, respectively,
31 associated with El Niño Southern Oscillation (ENSO), the Interdecadal Pacific Oscillation
32 (IPO) and the Pacific Decadal Oscillation (PDO), interacting with climate anomalies in the
33 South Atlantic and South Indian Ocean. CMIP5 models produce their own variability, but
34 perform better in simulating interannual rainfall variability, while QDV and IDV are largely
35 underestimated. These limitations can be partly explained by spatial shifts in core regions of
36 SA rainfall variability in the models. Most models reproduce the impact of La Niña on rainfall
37 at the interannual scale in SA, in spite of limitations in the representation of ENSO. Realistic
38 links between negative IPO are found in some models at the QDV scale, but very poor
39 performances are found at the IDV scale. Strong limitations, *i.e.* loss or reversal of these
40 teleconnections, are also noted in some simulations. Such model errors, however, do not
41 systematically impact the skill of simulated rainfall variability. This is because biased SST
42 variability in the South Atlantic and South Indian Oceans strongly impact model skills by
43 modulating the impact of Pacific modes of variability. Using probabilistic multi-scale
44 clustering, model uncertainties in SST variability are primarily driven by differences from one
45 model to another, or comparable models (sharing similar physics), at the global scale. At the
46 regional scale, *i.e.* SA rainfall variability and associated teleconnections, while differences in
47 model physics remain a large source of uncertainty, the contribution of internal climate
48 variability is increasing. This is particularly true at the QDV and IDV scales, where the
49 individual simulations from the same model tend to differentiate, and the sampling error
50 increase.

51

52 **Keywords** Southern African rainfall variability · Interannual to interdecadal timescales ·
53 Sea-surface temperature anomalies · Teleconnections · CMIP5 models

54

55 **1. Introduction**

56 Southern Africa (SA, south of 20°S) is known to be particularly vulnerable to climate change
57 due to a combination of a naturally high degree of climate variability and high reliance on
58 climate-sensitive activities, such as rain-fed agriculture (Conway et al. 2015). In particular,
59 during the main rainy season, *i.e.* austral summer (Nov–Feb, NDJF), SA rainfall has been
60 shown to vary over ranges of timescales from synoptic (3–7 days; *e.g.* Todd and Washington
61 1999; Hart et al. 2012; Macron et al. 2014) to decadal (≥ 10 years; *e.g.* Dyer and Tyson 1977;
62 Tyson 1981 1986; Mason and Jury 1997, Dieppois et al. 2016), as well as potential complex
63 interactions across timescales. For instance, Cook (2001) and Ratnam et al. (2014) proposed
64 that El Niño Southern Oscillation (ENSO) generates atmospheric Rossby waves in the Southern
65 Hemisphere, which could be responsible for longitudinal shifts of the South Indian
66 Convergence Zone (SICZ), where synoptic-scale rain bearing systems that affect southern
67 Africa, such as tropical-temperate troughs (TTTs), preferentially develop (Todd and
68 Washington 1999; Hart et al. 2012; Macron et al. 2014). Similarly, Dieppois et al. (2016) and
69 Pohl et al. (2018), highlighted that part of the non-linearity in the relationship between ENSO
70 and summer SA rainfall, which is prominent at the interannual timescale, could be explained
71 by interactions with the Interdecadal Pacific Oscillation (IPO) and the Pacific Decadal
72 Oscillation (PDO) at the quasi-decadal (8–13 years; QDV) and interdecadal (15–28 years; IDV)
73 timescales, respectively. These studies also suggested that ENSO-like shifts and modulations
74 of the Walker circulation in response to the IPO and PDO are interacting with regional ocean-
75 atmospheric circulations, such as the South Indian Ocean Dipole (Morioka et al. 2015), leading

76 to shifts in the SICZ and modulations of the TTT occurrence. However, despite the importance
77 of these decadal timescales in SA rainfall variability, and their impact on societies, little has
78 been done to examine the ability of global climate models, particularly those that constitute the
79 Coupled Model Intercomparison Project-phase 5 (CMIP5), to reproduce such processes on
80 interannual to interdecadal timescales.

81
82 Model-based studies in southern Africa have highlighted large differences between climate
83 models, especially in their estimates of historical rainfall (Hewitson and Crane 2006; Nikulin
84 et al. 2012; Kalogomou et al. 2013; Dieppois et al. 2015; Munday and Washington 2016 2018).
85 While models reproduce the annual cycle of rainfall reasonably well, there are large
86 discrepancies in rainfall amount, and in particular in austral summer (*e.g.* Dieppois et al. 2015;
87 Munday and Washington 2016 2018). As illustrated in Fig. 1a-b, most CMIP5 models
88 significantly overestimate summer-rainfall, especially in areas of greater rainfall such as the
89 north-eastern region of southern Africa (where more than 60% of models show an average wet
90 bias of 34 mm.months⁻¹ or +41%). However, long-term SA rainfall variability has been poorly
91 studied despite of the extensive use of CMIP5 models for climate impact assessment.

92
93 Some authors have proposed that part of such bias in SA rainfall could be explained by
94 significant model-dependency on the strength of the Angola Low amongst CMIP5 models
95 (Munday and Washington 2016; Lazenby et al. 2016), but underlying drivers of these model
96 uncertainties remain unclear. Such uncertainties in CMIP5 models could also be explained
97 through misrepresentations of the linkage between regional circulation and large-scale modes
98 of climate variability. This is, for instance, the case for ENSO (Dieppois et al. 2015), which has
99 major influences on SA rainfall variability (*e.g.* Ropelewski and Halpert 1987 1989; Lindsay
100 1988; Mason and Jury 1997; Rouault and Richard 2005; Kane 2009; Crétat et al. 2012; Ratnam

101 et al. 2014; Hoell et al. 2015; Dieppois et al. 2016). Dieppois et al. (2015) thus pointed out that
102 anomalous westward extensions of ENSO patterns in the CMIP5 models were leading to wet
103 biases in SA during El Niño events, as a response to anomalously continental locations of the
104 SICZ. This is consistent with recent findings from James et al. (2018), who identify too many
105 TTTs, and too much rainfall from TTTs in HadGEM3-GC2. Similarly, decadal ENSO-like
106 patterns related to the IPO and PDO, and their interactions with atmospheric regional
107 circulations, which also play an important role in SA rainfall variability (Dieppois et al. 2016;
108 Malherbe et al. 2016; Pohl et al. 2018), could potentially contribute to CMIP5 model
109 uncertainties over the region. Decadal rainfall anomalies have, for instance, been shown to
110 explain a large part of the persistent drought in this region between the 1960s and 1990s (*e.g.*
111 Richard et al. 2001; Rouault and Richard 2005; Dieppois et al. 2016; Malherbe et al. 2016; Pohl
112 et al. 2018).

113

114 At the global scale, decadal rainfall variance has been shown to be largely underestimated in
115 the CMIP3 and CMIP5 models (Ault et al. 2012). Decadal sea-surface temperature (SST)
116 variability is often underestimated in the Pacific (Ault et al. 2013; Laepple and Huybers 2014;
117 Henley et al. 2017; Power et al. 2017) and overestimated in the North Atlantic (Ba et al. 2014;
118 Menary et al. 2015). This suggests that future climate projections could poorly represent
119 decadal variability, and offer a limited view of prolonged drought and hydro-meteorological
120 risks. Underlying drivers of such model uncertainties however remain unclear, especially at
121 these timescales, and might be region-dependent (Hawkins and Sutton 2009; Deser et al. 2012).
122 So far, no study has attempted to address these issues in SA. Using a time-space approach based
123 on spectral analysis and a probabilistic clustering, this study then aims to: i) identify potential
124 key sources of uncertainties in the CMIP5 models at different timescales; ii) discuss the
125 respective contributions of different model physics and internal climate variability to the

126 CMIP5 model uncertainties at those timescales; iii) better understand processes driving SA
127 rainfall variability, especially using CMIP5 multimodel ensemble.

128
129 This paper is organized as follows. In section 2, the datasets and methods are described. In
130 section 3, we analyse the ability of CMIP5 models to simulate observed timescales of summer
131 SA rainfall variability. In section 4, we assess model skill to simulate global SST variability at
132 decadal timescales, and the teleconnections between SA rainfall and global SST. In section 5,
133 we discuss the potential uncertainties related to the sample sizes (*i.e.* length and number of
134 simulations per model), and the capability of each model, using longer-term model simulations.
135 We then show in section 6 how four contrasting CMIP5 models represent atmospheric bridges
136 linking the Pacific Ocean and SA. Finally, our main results are interpreted and discussed in
137 section 7.

138

139 **2. Data & Methods**

140 **2.1. Observations**

141 The Climatic Research Unit (CRU) dataset is used to compare observed and simulated summer
142 SA rainfall variability (Harris et al. 2014; Table 1). The summer-rain region, which is here
143 defined as the region where the wettest months occur in NDJF, extends to all the north-eastern
144 part of southern Africa (Fig. 1c). To optimally investigate summer-rainfall variability and its
145 teleconnections, a summer-rainfall index (SRI) has been constructed by averaging the values
146 over the summer region, as displayed in Fig. 1c. According to Dieppois et al. (2016), the quality
147 of the SRI is quite stable throughout the 20th century, as a satisfactory number of rain gauges
148 was always available over the region. In addition, very similar results were found using Global
149 Precipitation Climatology Centre full data reanalysis version 7.0 (Schneider et al. 2014).

150

151 To examine the summer teleconnections with global SSTs, we used the extended reconstructed
152 SST version 4 (ERSST.v4) of the National Climatic Data Centre (Huang et al. 2015; Table 1).
153 Version 4 does not use satellite data, and is thus coherent over the whole time period. It is not
154 affected by the cold SST bias induced by the use of satellite observations at the end of the 20th
155 century (Reynolds et al. 2002). Uncertainty related to the choice of the observed SST datasets
156 has been assessed in Dieppois et al. (2016), who compared the composite SST anomalies
157 associated with SA rainfall from ERSST.v4 to those obtained using the HadISST1 (Rayner et
158 al. 2003) and COBE SST2 (Hirahara et al. 2014) datasets: an agreement greater than 90%
159 between datasets was found regardless the timescale, ensuring the reliability of our reference
160 SST dataset.

161

162 As recommended in Zhang et al. (2013), the 20th Century Reanalysis version 2c (20CR.v2c;
163 Compo et al. 2006 2011) is used as reference to discuss the representation of atmospheric
164 bridges between the Pacific Ocean and SA (Table 1). Such atmospheric bridges are here
165 depicted through velocity potential (φ) and stream function (ψ) composite anomalies in the
166 lower and upper troposphere (850–600 and 400–150 hPa). The 20CR.v2c assimilates only
167 surface pressure, and uses monthly SST and sea ice distributions as boundary conditions. Such
168 a modelling and data assimilation strategy that remains constant over the entire time period
169 allows spectral decompositions in analysing atmospheric circulation across different timescales
170 with a reduced sensitivity to time-varying availability of observational datasets. The density of
171 the observational network, *e.g.* amounts of assimilated data, as well as the quality of the SST
172 field used as boundary conditions, remains nevertheless an intractable problem. This is likely
173 to reduce the quality of the reanalyses, and the consistency between its different members, for
174 the first decades of the period (Pohl et al. 2018). However, atmospheric composite anomalies
175 associated with SA rainfall from all reanalysis members were consistent and significantly

176 correlated with the ensemble mean, suggestive of weak inter-member uncertainty (Dieppois et
177 al. 2016).

178

179 ***2.2. CMIP5 model output***

180 Performances have been assessed against observations using historical runs from 28 CMIP5
181 models (Table 1), which simulate climate variability from the mid-19th century to the early 21st
182 centuries, and are driven by observed estimate of anthropogenic and natural forcings (Taylor et
183 al. 2012). Initialization schemes are model dependent. Models from the same institutions or
184 different institutions can share (successive) versions of the same atmospheric, oceanic, land
185 surface and sea-ice components, and, therefore use very similar physics for simulating some
186 parameterized processes of the climate system (Table 2). The spatial resolutions also change
187 from one model to another (Table 1). The ocean grids were interpolated on orthogonal
188 curvilinear grid in some models, making comparison difficult with regular grids, and have thus
189 been remapped on a regular 2°×2° resolution grid using bilinear interpolation.

190

191 To assess the contribution of internal climate variability, all calculations have been performed
192 on each individual member, giving a total of 95 simulations (Table 1). In addition, to test the
193 uncertainties associated with the sample sizes (*i.e.* length and number of simulations per model),
194 which might be limiting at decadal timescale, longer-term pre-industrial control (piControl)
195 simulations have been used in Section 5 (Table 1).

196

197 Model-simulated SRI has been calculated by averaging summer-rainfall amounts spatially in
198 each historical and piControl runs from the 28 CMIP5 models (Fig. 1c). The simulated summer-
199 rainfall region matched well with that observed, although their spatial extension sensibly varies
200 from one model to another (Fig. 1c).

201

202 **2.3. Timescales of variability and associated teleconnections**

203 In section 3, we first compare the significant timescales of observed SRI variability with those
204 simulated in the 95 members from the 28 selected CMIP5 models using fast Fourier transform
205 (FFT). Significance tests of the FFT spectrum assumes a red-noise background spectrum for
206 the null hypothesis, which is tested by 10,000 Monte Carlo simulations of first-order
207 autoregressive (AR[1]) processes (Ghil et al. 2002). We next compare the SRI variance
208 according to the three dominant timescales identified in observations (*i.e.* interannual: 2–8 year;
209 QDV: 8–13 year; IDV: 15–28 year; Dieppois et al. 2016) by submitting observed and simulated
210 time series to FFT band-pass filtering. To reduce trend effects (Wu et al. 2007), the SRI indices
211 are preliminary detrended using a locally weighted linear regression, with span equal to the
212 length of the data. We then compute the centered ratio of standard deviation (*rSD*), here
213 expressed as a percentage:

$$214 \textit{centered.rSD} = 1 - \frac{sd(SRI[obs]^t)}{sd(SRI[sim]^t)} \times 100 \quad (1)$$

215 where *sd* refers to the standard deviations of the time series, and *t* indicates the corresponding
216 timescales. Statistical significance of equality between observed and simulated variance is
217 estimated using a two-sided Fisher's *F* test at $p = 0.05$. The same procedure is then applied to
218 each grid-point over the SA region, and to global SST in section 4.

219

220 In section 4, we also assess the ability of CMIP5 models to simulate teleconnection between
221 SRI and global SSTs. After replicating the filtering procedure described above to SST datasets,
222 composite analyses are performed to construct typical states of global SSTs associated with SA
223 rainfall fluctuations. Two sets of SST anomalies are produced for each timescale, where the
224 SRI exceeds ± 1 standard deviation (*i.e.* wet and dry anomalies); the resulting composites thus
225 describe the difference in SST between wet and dry conditions over SA. Statistical significance

226 is estimated by testing the difference in mean between wet and dry SST anomalies using a two-
227 sided Student's t test at $p = 0.05$. When time series are serially correlated, the degrees of
228 freedom are adjusted by recalculating the “effective sample size” (N^{eff}). This is given by the
229 following approximation (Yue and Wang 2004):

$$230 \frac{N}{N^{\text{eff}}} = 1 + \frac{2}{N(N-1)(N-2)} \sum_{i=1}^t (N-i-1)(N-i-2)ts(i) \quad (2)$$

231 where N is the number of observations in the sample, $ts(i)$ is the serial correlation between ranks
232 of the observations for lag i , and t is the maximum time lag considered. This procedure has then
233 been replicated for piControl simulations in section 5, and to examine the performance of the
234 models to reproduce atmospheric bridges between the Pacific basin and SA in section 6. Note
235 that, while the present study aims at identifying climate processes associated with different
236 ranges of SA rainfall fluctuations, some non-linearity between SST anomalies associated with
237 wet and dry years only emerge at the interannual timescale (Fig. A1).

238

239 **2.4. Assessing and narrowing model uncertainties**

240 In sections 3 and 4, model performance is systematically assessed through Taylor diagrams
241 (Taylor et al. 2001). As mentioned in earlier studies (Hawkins and Sutton 2009; Deser et al.
242 2012), at the regional scale, model uncertainties are increasing at decadal timescales due an
243 increasing contributions of internal climate variability, adding to problems in model physics.
244 This enhances diversity in the CMIP5 simulations, as simulations of the same model are likely
245 to drift from one another, making meaningless the use of simple statistics (*e.g.* model mean and
246 spread). Similarly to previous studies (*e.g.* Jun et al. 2008; Knutti et al. 2010 2013), a clustering
247 approach has therefore been used to quantify the similarities between all models, and between
248 simulations of the same model without predefined assumption. The relative contributions of
249 model physics and internal climate variability could thus be discussed by assessing the inter-
250 simulation spread within the CMIP5 framework, while identifying recurrent patterns.

251
252
253
254
255
256
257
258
259
260
261
262
263
264
265
266
267
268
269
270
271
272
273
274
275

The similarities between the 95 simulated spatial patterns of SA rainfall variability, global SST variability and composite SST anomalies (*cf.* sections 2.3-4), have thus been quantified at each timescale using Ward’s agglomerative criteria applied to Euclidean distances (Ward 1963; Crétat et al. 2018). In addition, we used a multi-scale bootstrap approach, allowing for estimation of the probability of each cluster (Shimodaira 2002, 2004), to optimize the identification of recurrent and spatially coherent clusters within the multimodel ensemble (Fig. A2). To estimate approximately unbiased probability that a cluster appears in the replicate, 10,000 bootstrap resampling over 33 different spatial lengths of the data (2% to 180% of the spatial domain, *i.e.* 330,000 iterations) are used (Fig. A2). Randomly resampling the spatial domain with different sizes thus enables to reduce the uncertainty associated with the selected grid-resolution, and to balance the weight of different regions (*e.g.* Pacific vs. Atlantic). Only clusters showing $p \geq 0.90$ have been considered as robust (Fig. A2). Clusters have been named as #CL1[pr]- to n [pr]-int for rainfall variability at the interannual timescale, and as #CL1[pr] to n [pr]-QDV and IDV at the QDV and IDV timescales (abbreviation [sstvar] and [sstano] have been used for clusters of global SST variance and composite anomalies, respectively).

In addition, in section 5, we discussed the sampling uncertainties in simulating observed statistics using historical and the longer-term piControl runs. The capability to significantly simulate observed SRI variance and global SST teleconnections at the three different timescales has been calculated by replicating the procedure described in section 2.3 for every 113 year time-period through the course of historical and piControl runs. The Fisher F test of equal variance at $p = 0.05$ and Pearson’s spatial correlation have been used to quantify the capability to simulate rainfall variance and SST teleconnection, respectively.

276 **3. Summer SA rainfall variability**

277 *3.1. SRI variability*

278 The ability of CMIP5 models to simulate SRI variability (including its timescales and variance)
279 is displayed in Fig. 2. Corroborating Dieppois et al. (2016), observed SRI exhibits three
280 significant timescales of variability over the 20th century (Fig. 2a): interannual (2–8 years),
281 QDV (8–13 years) and IDV (15–28 years). Simulated and observed FFT spectra strongly differ
282 (Fig. 2a). There are also large differences between FFT spectra from different models, and
283 between simulations from the same model (Fig. 2a), indicating that CMIP5 simulations tend
284 to produce their own variability.

285

286 However, as illustrated in Fig. A3, most models, and almost all institutions, can produce
287 significant variability within the interannual, QDV and IDV timescales, suggesting that
288 differences in simulated FFT spectra mostly result from internal climate variability, different
289 resolutions and physics. The ratios of standard deviation between CMIP5 models and
290 observation have thus been calculated at the three different timescales (Fig. 2b). CMIP5
291 models, perform better in simulating SRI variability at the interannual timescale (-6% average
292 bias) than at the QDV and IDV timescales (-15 and -37% average bias; Fig. 2b). At the
293 interannual timescale, more than 50% of the simulations show similar variance to observations
294 (Fig. 2b), while significant underestimations and overestimations are detected in 35 and 14%
295 of model simulations, respectively (Fig. 2b). At the QDV and IDV timescales, only about 30
296 and 14% of the CMIP5 simulations, respectively, show significant variance close to
297 observation (Fig. 2b). These simulations always correspond to models producing realistic
298 rainfall variance at the interannual timescale (Fig. 2b), suggesting cross-linkages between
299 timescales in the model errors. Biases in simulating SRI variance are indeed proportionally
300 stronger from the interannual to IDV timescales, especially for model simulations

301 underestimating SRI interannual variability (box plots on Fig. 2b). 51 and 77% of model
302 simulations thus significantly underestimate SRI QDV and IDV, respectively (Fig. 2b).

303

304 ***3.2. Core regions of summer SA rainfall variability***

305 *3.2.1. Observations*

306 Observed interannual rainfall variability explains approximately 70% of the total variance on
307 average over SA (Fig. 3a). As for the raw data, interannual rainfall variability is clearly more
308 pronounced in the northern and eastern regions (Fig. 3a), where summer-rainfall amounts are
309 greater (Fig. 1a). At the QDV and IDV scales, which both can express more than 10% of the
310 total variance over SA, similar patterns of rainfall variability are identified (Fig. 3a). The QDV
311 is more pronounced on the eastern coastal regions of South Africa, but does not contribute much
312 to total rainfall variability northeast of the central plateau (SA highlands; Fig. 3a), while the
313 IDV is more pronounced in this region (Fig. 3a). In addition, according to earlier studies (Tyson
314 1981 1986; Mason and Jury 1997; Dieppois et al. 2016; Malherbe et al. 2016), the QDV can
315 explain up to 26% of the total rainfall variance over the southwestern regions (Fig. 3a).

316

317 *3.2.2. Model performances*

318 CMIP5 models show good skills in simulating spatial patterns of summer SA rainfall
319 variability at the interannual timescale (Fig. 4a). Spatial correlations between CMIP5
320 simulations and observation often exceed 0.7 (up to ≥ 0.9), while the normalized mean bias is
321 lower than 1 (Fig. 4a). Model skills remain moderately good at the QDV and IDV timescales
322 ($0.5 \leq r \leq 0.85$), although these scores substantially drop in some simulations at the IDV scale
323 (approaching 0; Fig. 4c). Although some models substantially overestimate spatial variability
324 at each timescale, simulated patterns of rainfall variability are often close to the observed one,
325 suggesting similar patterns than in observation (Fig 4a-c).

326

327 3.2.3. CMIP5 model diversity

328 Multi-scale bootstrapped clustering has been used to identify the recurrent and spatially
329 coherent patterns in simulating summer SA rainfall variability within the CMIP5 multimodel
330 ensemble. While 13 significant clusters are identified at the interannual scale, model diversity
331 substantially increases at the QDV and IDV timescales with 28 and 21 significant clusters,
332 respectively (Fig. 4d).

333

334 At the interannual timescale, clusters primarily refer to the different models and institutions
335 (Fig. 4d). Different parameterizations of the LMDZ atmospheric model however lead to
336 differentiations of the distinct versions of the IPSL model (Fig. 4d). Similarly, CMCC-CESM,
337 which includes carbon cycle feedbacks, differs from other CMCC models (Fig. 4d). Models
338 from different institutions sharing the same atmospheric model (or different versions; Table 2)
339 also tend to be clustered together at the interannual timescale (*e.g.* ACCESS1-0 and MOHC,
340 CMCC-CESM and MPI, or CESM1-BCG and CCSM4; Fig. 4d). In addition, some models
341 from different institutions (*e.g.* ACCESS1-3, CSIRO-Mk3-6-0 and MIROC5), are also
342 regrouped (Fig. 4d). Although the similarities between these models could not be explain here
343 through similarities in model physics, all these models are found to overestimate interannual
344 SRI variability (Fig. 2).

345

346 At the QDV and IDV scales, individual simulations from the same or comparable models,
347 gradually differentiate, increasing cluster diversity (Fig. 4d). For instance, four significant
348 clusters emerge from CNRM-CM5 at the QDV scale, and this is also the case for most models
349 (Fig. 4d). ACCESS1-3, CSIRO-Mk3-6-0 and MIROC5, which all overestimate interannual SRI
350 variability, still have some simulations clustered together at the QDV and IDV timescales (Fig.

351 4d). This differentiation between simulations of the same models suggests larger contributions
352 of internal climate variability to model biases. The different clusters could also still partly
353 discriminate different model physics. This is confirmed in Fig. A4, as correlations between
354 simulations from the same models decrease from interannual to IDV timescales, but remain
355 stronger than correlations between different models.

356

357 *3.2.4. Simulated spatial patterns of SA rainfall variability*

358 Such diversity of simulated SA rainfall variability at the three different timescales is illustrated
359 in Fig. 5. For clarity, names of model simulations describing each clusters are provided in Fig.
360 A5.

361

362 According to observation, CMIP5 models generally simulate greater variability in the NE than
363 in the SW regions regardless of the timescale (Fig. 5). However, slight misrepresentations of
364 core regions of SA rainfall variability help explaining biases detected in SRI variability at all
365 timescales. CMIP5 simulations overestimating SRI variability (#CL1[pr]-int, #CL1-2[pr]-
366 QDV, #CL1, 6[pr]-IDV; Fig. A5) show very realistic patterns, but overestimate rainfall
367 fluctuations in the north-west of the summer-rain region (Fig. 5a-c). In NASA-GISS models
368 (#CL13[pr]-int, #CL5[pr]-QDV, #CL12[pr]-IDV; Fig. A5), rainfall variability is strongest in
369 the eastern coastal regions of SA at all timescales, hence large underestimations further inland
370 (Fig. 5a). At the interannual and QDV scales, MPI models and CMCC models (#CL10[pr]-int
371 and #CL25[pr]-QDV; Fig. A5) simulate too strong rainfall variability in the western region,
372 and underestimate it further east (Fig. 5a). Interestingly, the best performing simulations of SRI
373 variability (#CL2, 6, 7, 10[pr]-int, #CL21, 24[pr]-QDV; Fig. A5) also show significant biases
374 in rainfall variability over SA (Fig. 5a).

375

376 In summary, although the NE-SW gradient in SA rainfall variability is generally well
377 reproduced for all timescales, slight shifts in core regions of SA rainfall variability could
378 explain part of the biases in simulating SRI variability. This leads to great model diversity,
379 suggesting contrasted links with large-scale and/or regional circulation patterns in CMIP5.

380

381 **4. Interannual to interdecadal global SST variability and teleconnections with SA** 382 **rainfall**

383 We examine here the ability of CMIP5 models to simulate global modes of SST variability at
384 these timescales, and their teleconnections with SA rainfall.

385

386 ***4.1. Observations***

387 In observations, ENSO is the dominant mode of global SST variability at the interannual
388 timescale (Mann and Park 1994; Klein et al 1999; Ghil et al. 2002; Sarachick and Cane 2010;
389 De Viron et al. 2013), hence significant fluctuations in the equatorial Pacific at $p = 0.05$ (Fig.
390 3b). Positive SRI anomalies are thus primarily related to La Niña events, which are associated
391 with cooler tropical Indian Ocean SSTs (Fig. 3c). Observed interannual SRI variability is also
392 related to the South-West Indian Ocean SST dipole (Reason 1998; Reason and Mulenga 1999;
393 Reason 2001; Behera and Yamagata 2001; Washington and Preston 2006; Hoell et al. 2017,
394 2018), the South Atlantic SST dipole (Fauchereau et al. 2003; Hermes and Reason 2005;
395 Vigaud et al. 2009), and SST fluctuations reminiscent of Benguela Niños/Niñas (Lubbecke et
396 al. 2010; Rouault 2012; Reason and Smart 2015).

397

398 The pattern of SST variability at the QDV timescale is similar to that of ENSO (Tourre et al.
399 1999 2001 2005; Fig. 3b). Wet conditions in SA are once again related to cold anomalies in the
400 east Pacific flanked by a horseshoe pattern of opposite sign, confirming the results by Dieppois

401 et al. (2016). This is consistent with the negative IPO pattern after the definition provided by
402 Power *et al.* (1999), and revisited by Di Lorenzo et al. (2015). This negative IPO occurs
403 concomitantly with cold anomalies in the tropical Indian Ocean (Fig. 3c), as highlighted in
404 Allan et al. (2003). Dipole SST anomalies in the South Atlantic Ocean and the SW Indian Ocean
405 have also been related to SA rainfall at this timescale, in response to shifts in the atmospheric
406 circulation (Venegas et al. 1996 1997; Dieppois et al. 2016). Climate anomalies in the SW
407 Indian Ocean were however clearer in Jury et al. (2014) and Morioka et al. (2015), using a
408 shorter period and other datasets.

409

410 As shown in Tourre et al. (1999 2001 2005), SST variability is particularly pronounced in the
411 North Pacific at the IDV timescale (Fig. 3b). At this timescale, Pacific SST anomalies
412 associated with SRI fluctuations display a horseshoe pattern, which is reminiscent of the PDO
413 (*e.g.* Mantua et al. 1997; Mantua and Hare 2002; Newman et al. 2016). SRI fluctuations have
414 also been connected to SST anomalies in the South Atlantic and Indian Oceans at the
415 interdecadal timescale (Dieppois et al. 2016; Pohl et al. 2018). We thus note cold anomalies in
416 the tropical Indian and South Atlantic Oceans, and warm anomalies in the extra-tropics (Fig.
417 3c). These regional SST anomalies in the adjacent oceans could be associated with enhanced
418 atmospheric circulation in the Southern Hemisphere (Venegas et al. 1996 1997; Dieppois et al.
419 2016), and to the Southern Annular Mode (SAM; Ciasto et al. 2011; Malherbe et al. 2014 2016).

420

421 ***4.2. Model performances***

422 The performance of CMIP5 models for simulating spatial patterns of global SST variability at
423 the three different timescales are summarized in Fig. 6a. Their respective skills in simulating
424 global SST anomalies associated with SA rainfall variability are displayed in Fig. 6b. Model
425 performances in simulating global SST variability are reasonably good at the interannual

426 timescale (spatial correlation comprised between 0.45 and 0.75 against observations).
427 Correlations gradually decrease at the QDV ($0.3 < r < 0.7$) and IDV ($0.1 < r < 0.65$) scales (Fig.
428 6a-b). For the teleconnections between SA rainfall and global SST (Fig. 6b), most models show
429 correlations greater than 0.4 at the interannual timescale. Correlations are weaker at the QDV
430 scale ($-0.6 < r < 0.7$) and weaker still at the IDV scale ($-0.4 < r < 0.4$; Fig. 6a-b).

431
432 Global SST variability can be too strong in CMIP5 models regardless the timescale (Fig. 6a).
433 However, some regions, such as the Arctic and the Southern Ocean, strongly suffer from large
434 uncertainties in observation due to data scarcity (Hirahara 2014; Huang et al. 2016). More
435 specifically for SA rainfall, the teleconnections with global SST show very contrasted skills at
436 all timescales, suggesting large model diversity.

437

438 ***4.3. Model diversity***

439 The number of significant clusters of global patterns of SST variability (14, 13 and 15 from the
440 interannual to IDV) and of global SST anomalies associated with SA rainfall (22, 24, 19) is
441 almost constant regardless the timescale (Fig. 6c). The clusters of global SST variability
442 patterns mostly discriminate resembling models (sharing some components or
443 parameterizations; Table 2), in spite of some exceptions (like the different versions of the IPSL
444 model). The situation is far less clear for global SST–SA rainfall teleconnections, especially at
445 the QDV and IDV scales, where intra-ensemble similarities are as much or more important than
446 inter-model similarities (Fig. A6). At these timescales, all CMIP5 model ensembles produce
447 different clusters of global SST-SA rainfall teleconnections, suggesting major contributions of
448 internal climate variability. For instance, CSIRO-Mk3-6-0 simulations, which were converging
449 at the interannual scale, drift into 6 and 5 different clusters at the QDV and IDV scales (Fig.
450 6c).

451

452 ***4.4. Simulated global SST variability, and teleconnections with SA rainfall***

453 CMIP5 model diversity in simulating global patterns of SST variability and SST-SA rainfall
454 teleconnection is illustrated in Figs. 7 and 8, respectively. For clarity, names of model
455 simulations describing each clusters are provided in Fig. A5.

456

457 At the interannual timescale, ENSO patterns are extending too far west and too tightly confined
458 to the equator (AchutaRao and Sperber 2006; Capotondi et al. 2006, Lin 2007; Guilyardi et al.
459 2009; Fig. 7a), which could substantially impact SA rainfall variability, as suggested in
460 Dieppois et al. (2015). Most models link wet conditions in SA to La Niña SST anomalies in the
461 Pacific, and to cold tropical Indian Ocean (#CL4, 6, 9, 10[sstano]-int; Figs. 8a, A5). However,
462 simulated La Niña SST anomalies extend too far west (*e.g.* #CL4, 6, 9[sstano]-int), and/or are
463 too confined to the equatorial latitudes (#C10, 14[sstano]-int; Fig. 8a). These models also
464 simulate the teleconnections with SA rainfall in the South Atlantic and South Indian Oceans
465 (Fig. 8a), but SST anomalies there are too strong, given the systematic overestimations of SST
466 variability (Fig. 7a). This systematic overestimations of SST variability could be due to
467 limitations in simulating wind-stress in the mid-latitude and subtropical regions, which has been
468 reported too strong by as much as 55% in CMIP3 and CMIP5 (Lee et al. 2013). These biases
469 in the adjacent oceans have major implication for SA rainfall variability. As illustrated in Figure
470 9, even though most simulations (~60%) reproduce the main teleconnection with ENSO at
471 interannual scale, only half of them lead to realistic representation of SA rainfall variability.
472 This is because ENSO-induced large-scale climate anomalies are almost always associated with
473 biased regional climate anomalies over the South Atlantic and South (and Tropical) Indian
474 Oceans (Fig. 9), which can substantially modulate their impact on the continent (Hoell et al.
475 2017).

476

477 In other models (*e.g.* #CL7[sstano]-int.; Fig. A5), SA rainfall variability is not significantly
478 related to ENSO at the interannual scale (Fig. 8a). In these models, interannual SRI variability
479 is primarily linked to the South Indian and South Atlantic Oceans (Fig. 8a), denoting changes
480 in the regional atmospheric circulation, *i.e.* changes in wind-stress modifying sensible and latent
481 heat fluxes (Fauchereau et al. 2003). Such regional changes in SSTs could also be associated
482 with the SAM (Ciaasto et al. 2011), whose the component driven by ENSO (including the impact
483 on austral summer-rainfall) is not captured in most CMIP5 models (Lim et al. 2016).
484 Interestingly, although those regional climate anomalies are systematically biased, they can lead
485 to good representation of SA rainfall variability (Fig. 9), suggesting error compensations.
486 Underestimations of ENSO anomalies in austral summer could however be at least partly
487 explained by misrepresentations of the seasonality in ENSO variability in some models (Fig.
488 A7). For instance, ENSO activity is peaking between March and August in IPSL models, and
489 is slightly delayed in ACCESS1-3 (Fig. A7). This is not true for CCSM4 and CESM-BCG,
490 which show realistic seasonal timing in ENSO activity, even though largely overestimated (Fig.
491 A7). In some CCSM4 simulations (#CL8[sstano]-int; Fig. A5), wet conditions occur during El
492 Niño events (Fig. 8a), *i.e.* a reversed-sign association compared to observations.

493

494 At the QDV timescale, tropical SST variability in the central Pacific is far too weak in most
495 CMIP5 models (Fig. 7b), suggesting large underestimations of IPO variability. In addition,
496 according to Henley et al. (2017), CMIP5 models locate IPO variability too far west (#CL1, 2,
497 4, 8 and 12[sstvar]-QDV; Figs. 7b, A5). Some models thus simulate negative IPO anomalies
498 associated with cold anomalies in the tropical Indian Ocean (#CL1, 21, 24[sstano]-QDV; Figs.
499 8b, A5). A skilful representation of the IPO teleconnection is however rarely associated with a
500 good representation of SA rainfall variability (Fig. 9). We also systematically found SST dipole

501 anomalies in both the South Atlantic and South Indian Oceans (Fig. 8b). Interestingly, although,
502 these climate anomalies in the adjacent oceans are biased in most models, they can lead to good
503 reproduction of SA rainfall variability (Fig. 9). This suggests error compensations at the QDV
504 scale also. Some models simulate weak or even reversed relationships between SA rainfall and
505 Pacific SSTs (Fig. 2b). For instance, in #CL11 [sstano]-QDV (Fig. A5), wet conditions are
506 linked to positive IPO (Fig. 8b).

507

508 At the IDV timescale, the PDO variability is systematically confined to the North Pacific in
509 most CMIP5 models (Fig. 7c), while it should extend further in the tropics in response to ENSO
510 forcing (Schneider and Cornuelle 2005). Very few simulations, which are the best performing
511 in simulating SRI variability at this timescale (Fig. 2b), link wet conditions over SA to negative
512 PDO anomalies (#CL1-2[sstano]-IDV; Figs. 8c, 9, A5). These simulations also simulate cold
513 (warm) SST anomalies in the tropical (extra-tropical) Indian and South Atlantic Oceans (Fig.
514 8c). However, the same simulations tend to link SA rainfall to decadal ENSO-like SST
515 anomalies, reminiscent of negative IPO in the tropical Pacific Ocean (Fig. 8c). Indeed, many
516 simulations overestimate IPO-like variability in the equatorial Pacific at the IDV scale (*e.g.*
517 #CL1, 11[sstvar]-IDV; Figs. 7c, A5). Although this could highlight systematic biases in CMIP5
518 models (*e.g.* Fleming and Anchukaitis 2016), concomitance between IPO and PDO patterns
519 might arise from internal climate variability. In-phase variability of these low-frequency modes
520 is very rare, and has not been observed at this timescale over the instrumental period (Fig. 3b-
521 c).

522

523 **5. Sample size uncertainties and model capabilities**

524 With an increasing contribution of internal climate variability, regional model evaluations could
525 be influenced by the sample sizes (*i.e.* length and number of simulations per model). This is

526 particularly true at decadal timescales, where historical runs only capture ~14 and ~7 life cycles
527 of QDV and IDV, hence limiting the chance to match the observed “realisation”. In this section,
528 we thus discuss the capability of each model by quantifying the chance to reproduce SRI
529 variance and its global SST teleconnections for every 113 year time-period though the course
530 of all historical runs and using the longer-term piControl simulations (Fig. 10). The number of
531 samples used to quantify the model capabilities is not constant, and should be used as an
532 indicator of robustness (Fig. 10).

533

534 At the interannual timescale, half of the CMIP5 models show very good capability ($> 80\%$) to
535 significantly simulate SRI variance equal to observation in historical and piControl runs (Fig.
536 10a). In addition, model capabilities are most of the time weaker in piControl runs than
537 historical runs (Fig. 10a), suggesting that interannual SA rainfall variability is strongly
538 modulated by internal climate variability in longer runs. The capability to simulate significant
539 similar SRI variance between models and observation progressively decreases at the QDV and
540 IDV timescales (Fig. 9a). At the QDV timescale, ~75 and ~90% of CMIP5 models show
541 moderate to low capability in historical and piControl runs, respectively (Fig. 9a). At the IDV
542 timescale, a third and half of the CMIP5 models show some capability using historical and
543 piControl runs, respectively (Fig. 9a). At the QDV and IDV scales, model capabilities are also
544 generally greater in piControl runs than in historical runs (Fig. 9). This suggests that, at these
545 decadal timescales, better performance could be obtained in many models using longer runs (or
546 large-ensembles, which also account better for internal climate variability).

547

548 More mixed results are identified when analysing simulated teleconnections between SRI and
549 global SST anomalies. At the interannual timescale, 50% and 70% of CMIP5 models show
550 moderate to good capability in historical and piControl runs, respectively (Fig. 9b). Better

551 performance could have thus been found at the interannual scale using longer runs (or large-
552 ensembles). Similar results are found at the QDV timescales, even if very few models show
553 good capabilities. Model capabilities are however insensitive to the sample sizes, and are
554 always null, at the IDV timescale (Fig. 10b).

555
556 Interestingly, capabilities in simulating global SST-SA rainfall teleconnection are always
557 weaker than in SRI variance, which are generally greater at all timescales (Fig. 9a-b). This
558 suggest that misrepresentations of atmospheric bridges between the Pacific and SA, and its links
559 to the regional circulation (cf. Sect. 4.4), remain even through the course of piControl runs, and
560 are very little sensitive to internal climate variability. In this regard, GFDL-CM3 could be
561 considered as a reference in simulating both summer SA rainfall and their teleconnections at
562 the interannual timescale (Fig. 10a-b). Some models, such as CSIRO-Mk3-6-0 and, in
563 particular, MPI-ESM-LR, provide good capabilities to portray consistent interannual to QDV
564 fluctuations in both teleconnections and SRI variability (Fig. 10a-b).

565

566 **6. Atmospheric bridges**

567 *6.1. Observed atmospheric anomalies associated with SRI variability*

568 Observed atmospheric bridges between the Pacific and SA are examined through velocity
569 potential and stream function composite anomalies in the lower and upper troposphere (Fig.
570 11).

571

572 At the interannual timescale, La Niña SST events (which favour wet conditions over SA; Fig.
573 3c), are associated with large-scale lower-layer convergence over the western Pacific, and
574 divergence over the eastern Pacific, and reverse signals in the upper troposphere (Fig. 11). This
575 denotes conditions favourable to large-scale ascending motion over the Maritime Continent and

576 subsiding motions in the eastern Pacific, which is consistent with a westward shift and
577 intensification of the Walker circulation. According to Hoell et al. (2015), changes in vertical
578 winds and convection over the western Pacific result in tropospheric diabatic heating, which in
579 turn force a Gill-Matsuno response over the Indian Ocean basin and surrounding continents
580 (Fig. 11). The Gill-Matsuno response is materialized in the lower troposphere by significant
581 cyclonic circulation poleward and westward of the anomalous diabatic heating over the
582 Maritime Continent, while anticyclonic circulation is detected in the upper layers (Fig. 11). In
583 the Southern Hemisphere, this initiates a Rossby wave-train between the tropics and SA
584 (Hoskins and Ambrizzi 1993; Cook 2001), thereby evidenced by an anticyclonic ridge (Fig.
585 11). This contributes to an enhancement of the South Atlantic High. Dieppois et al. (2016)
586 argued that westerlies driven by the South Atlantic High then converge with easterlies from the
587 Indian Ocean, leading to ascending motions and convection in SA (Fig. 11). This pattern also
588 corresponds to a westward shift of the SICZ, favouring wet conditions in SA.

589

590 Similar mechanisms are identified at the QDV and IDV scales, where both negative IPO and
591 PDO anomalies are associated with a westward shift and intensification of the Walker-type
592 circulation, as well as a Gill-Matsuno response over the Indian Ocean basin (Fig. 11). However,
593 at the QDV timescale, the resulting Rossby wave-train shows a quasi-meridional propagation,
594 and acts to enhance the South Indian High (Fig. 11). This promotes easterly moisture flux from
595 the Indian Ocean (Dieppois et al. 2016), and convergence with south-easterly fluxes from the
596 Atlantic (Fig. 11), increasing rainfall over SA.

597

598 At the interdecadal timescale, atmospheric anomalies are much weaker, consistently with the
599 lower contributions of IDV to SA rainfall variability (Pohl et al. 2018). There, the Rossby wave-
600 train, evidenced by cyclonic circulation over subtropical SA, and anticyclonic circulation

601 further north (Fig. 11), modulates the regional circulation over SA. At the same time, significant
602 changes in the meridional circulations take place in the Southern Hemisphere, discernible as
603 alternating cyclonic and anticyclonic circulations in the extra-tropics (Fig. 11). Dieppois et al.
604 (2016) argued that such anomalies could help to enhance both the South Atlantic and South
605 Indian Highs, and potentially the SAM (Malherbe et al. 2016), which then favours convergence
606 and ascending motions over SA (Fig. 11).

607

608 ***6.2. Atmospheric anomalies associated with SRI variability in CMIP5 models***

609 Fig. 12 displays circulation composite anomalies in the lower troposphere as simulated by four
610 CMIP5 models with contrasted performances according to section 5.

611

612 In some models, neither rainfall variability nor their SST teleconnections are adequately
613 simulated (Fig. 10). In GISS-E2-R-CC, for instance, underestimations of La Niña SST
614 anomalies at the interannual timescale lead to a weak response of the atmosphere. Significant,
615 but far too weak, ascending motions are identified over the western Pacific, and subsidence
616 occurs over the eastern Pacific (Fig. 12). This is consistent with a westward shift and
617 intensification of the Walker circulation, but the associated Gill-Matsuno response over the
618 Indian Ocean is far too weak (Fig. 12). At the QDV and IDV scales, none of these circulation
619 anomalies are simulated (Fig. 12). This is due to major difficulties in simulating IPO and PDO
620 variability in the equatorial Pacific (Figs. 8, 9). Large underestimations of ENSO variability,
621 which is a common feature in NASA-GISS models (Fig. A7), leads to underestimate SRI
622 variability.

623

624 In other models, rainfall variability at the interannual and QDV timescales is adequately
625 reproduced, but as a response to different large-scale ocean-atmospheric processes (Fig. 10). In

626 IPSL-CM5B-LR, for instance, the relationship between SA rainfall and ENSO is reversed, and
627 consists of an eastward shift in the Walker circulation. Southward shifts of the South Atlantic
628 and South Indian Highs are also identified, as well as ascendance over the eastern coast of
629 Africa, potentially associated with warm SST there (Fig. 12). This increases rainfall over SA.
630 At the QDV and IDV scales, none of the observed circulation anomalies are simulated (Fig.
631 12), due to unrealistic IPO and PDO variability (Figs. 7-8). Rainfall QDV is therefore not
632 directly influenced by the Pacific Ocean, but by anomalously strong cyclonic circulations in the
633 subtropics.

634

635 GFDL-CM3 is the best performing model at the interannual timescale (Fig. 10). The westward
636 shift and intensification of the Walker circulation, as well as the Gill-Matsuno response over
637 the Indian Ocean are well simulated (Fig. 12). The intensity and the location of the South
638 Atlantic High, and thus convergence and ascendance over SA (*i.e.* the SICZ activity), fluctuate
639 from one simulation to another (Fig. 12). Similarly, contrasting performances are obtained over
640 the Pacific Ocean at the QDV and IDV timescales (Fig. 12): negative IPO-like and PDO-like
641 circulation anomalies are detected in one simulation only. At these timescales, rainfall
642 variability is primarily driven by enhanced activity in the subtropical Highs in the Southern
643 Hemisphere, in approximate agreement with observations (Fig. 12).

644

645 MPI models perform well at the interannual and QDV timescales (Fig. 10). In MPI-ESM-LR,
646 the westward shift and intensification of the Walker circulation associated with wet conditions
647 in SA is realistic in all simulations at both timescales (Fig. 12). However, at the interannual
648 timescale, the Gill-Matsuno response over the Indian Ocean in response to diabatic heating
649 anomalies over the western Pacific is not reproduced (Fig. 12): this may reflect Indian Ocean
650 SSTs, which are too cold, but further work is needed here. In MPI models, interannual rainfall

651 variability is then not directly linked to the Pacific Ocean, but to regional changes in the South
652 Atlantic and South Indian Highs (Fig. 11), which could be related to the SAM (Ciasto et al.
653 2011). At the QDV timescale, the Gill-Matsuno response is simulated too far west, and is
654 reversed compared to observation (Figs. 11-12), consistently with too cold SSTs over the
655 Maritime continent (Fig. 8). Interestingly, strong anomalous Gill-Matsuno responses (*e.g.*
656 *r1i1p1*) lead to overestimate SA rainfall QDV, while weak anomalous Gill-Matsuno response
657 (*e.g.* *r3i1p1*) lead to underestimations (Figs. 2, 12).

658

659 Taken together, the results of this section show that, while atmospheric bridges between the
660 Pacific Ocean and SA are crucial at all timescales in the observations, only few CMIP5 models
661 are able to reproduce it. In some models, simulated rainfall in SA is likely to be associated with
662 error compensations and strongly biased large-scale mechanisms even in cases where regional-
663 scale properties are realistically reproduced.

664

665 **7. Discussion & Conclusion**

666 This study is a first assessment of CMIP5 model performances in simulating SA rainfall
667 variability and its teleconnections with large-scale modes of variability at different timescales.
668 Historical runs from 28 models, and their associated piControl run ensembles, have been used
669 to document the weight of sampling errors and internal climate variability.

670

671 Firstly, we examined the ability of CMIP5 models to simulate realistic summer SA rainfall
672 variability, which exhibits three major timescales in observation (Dieppois et al. 2016):
673 interannual (2–8 years), QDV (8–13 years) and IDV (15–28 years). CMIP5 models produce
674 their own variability, but tend to perform better in simulating interannual timescales of SRI
675 variability. Indeed, most models strongly underestimate rainfall variability at the QDV and IDV

676 scales, suggesting a limited view of prolonged drought and hydro-meteorological risks in
677 CMIP5 models over SA. Highest skills in simulating SRI QDV and IDV are however obtained
678 with best performing models at the interannual timescale, suggesting cross-linkages in model
679 biases between timescales which could be used to improve the future generations of climate
680 models. These limitations in simulating SRI variability are partly due to spatial shifts in the
681 core regions of rainfall variability.

682

683 Secondly, CMIP5 model performances in portraying global SST variability at the three different
684 timescales was assessed, as well as their teleconnections with SA rainfall. In observation, wet
685 rainfall conditions over SA are associated with cold SSTs in the Pacific, mostly driven by
686 ENSO, the IPO and the PDO, which interact with regional climate anomalies in the South
687 Atlantic and South Indian Ocean (Dieppois et al. 2016; Pohl et al. 2018). Most models
688 reproduce La Niña effects on rainfall at the interannual timescale, in spite of biases in the
689 representation of ENSO (*e.g.* AchutaRao and Sperber 2006; Guilyardi et al. 2009). At the QDV
690 timescale, some models succeed in reproducing the association between the IPO and SA
691 rainfall, but IPO variability is systematically too weak, and extends too far west (Henley et al.
692 2017). Similarly at the IDV timescale, very few models reproduce negative PDO anomalies.
693 Yet, good performances in simulating the large-scale teleconnections with the Pacific do not
694 systematically lead to good representation of SA rainfall variability. This is because Pacific
695 modes of variability are most of the time associated with biased regional climate anomalies in
696 the adjacent oceans to SA, which, according to Hoell et al. (2017), can substantially modulate
697 their impact on the continent.

698

699 Some CMIP5 simulations do not reproduce, or even significantly reverse, the average link
700 between SA rainfall and Pacific SST variability at the interannual and QDV scales. Even though

701 this result suggests strong model limitations, such an unlikely configuration has already been
702 observed in rare occasions: during the exceptionally strong El Niño event of 1997/98, for
703 instance (Lyon and Mason 2007). In IPSL models and ACCESS1-3, such an unlikely
704 association between SA rainfall and El Niño anomalies could be due to errors in modelling the
705 seasonality of ENSO (Fig. A7). CMIP5 model limitations in fully-capturing the relationship
706 between the SAM and ENSO, and their combined impact on summer-rainfall in the Southern
707 Hemisphere, could also be crucial, as suggested in Lim et al. (2016). However, such errors do
708 not systematically impact the realism of simulated rainfall variability here. This is because of
709 error compensations, mostly resulting from substantial overestimation of SST variability in the
710 South Atlantic and South Indian Oceans, leading to appropriate simulations of SA rainfall
711 variability.

712

713 All together these results also highlight the potential importance of the South Atlantic and
714 Indian Ocean SSTs for SA rainfall, as suggested in earlier studies (Nicholson and Kim 1997;
715 Reason 1998 2001; Reason et al. 1999; Hoell et al. 2015, 2017, 2018; Morioka et al. 2015), and
716 in modulating the skills of CMIP5 models. They also emphasize the need for process-oriented
717 studies rather than merely descriptive work for model evaluation, since statistically coherent
718 regional variability can be obtained from biased large-scale teleconnections and mechanisms.
719 This issue is of crucial importance for operational seamless predictions and future climate
720 projections (*e.g.* Mason 1998; Landman and Beraki 2012; Beraki et al. 2014; Landman et al
721 2017).

722

723 Thirdly, the respective contributions of model errors and internal climate variability to overall
724 uncertainties have been disentangled using probabilistic multi-scale clustering. This new
725 methodology is strongly recommended for future model evaluation studies at regional and

726 decadal scales to assess and narrow the impact of internal climate variability. At the global
727 scale, model uncertainties in SST variability are primarily driven by differences from one model
728 to another. At the regional scale, *i.e.* SA rainfall variability and associated teleconnections,
729 model uncertainties are also mainly related to differences in model physics at the interannual
730 timescale. At the QDV and IDV scales, however, individual simulations from the same models,
731 or comparable models, progressively differentiate, which, consistently with Keenlyside et al.
732 (2008), suggests larger contributions of internal climate variability. Uncertainties related to the
733 sample size (length and number of simulations) have also been assessed using piControl runs,
734 and suggest that better performances could be obtained, at least on interannual and QDV scales,
735 in many CMIP5 models using longer-runs. Better impact-assessment of future prolonged
736 drought and hydro-meteorological risks over SA could therefore be obtained using large-
737 ensemble (*e.g.* Kay et al. 2015).

738

739 **Acknowledgements**

740 ERSST.v4, 20CR.v2, GPCC.v7 and COBE SST2 data were provided by the
741 NOAA/OAR/ESRL PSD, Boulder, Colorado, USA, from their website at
742 <http://www.esrl.noaa.gov/psd/>. The CRU TS 3.24.1 rainfall field were available from the Centre
743 for Environmental Data Archival (CEDA) at
744 <http://catalogue.ceda.ac.uk/uuid/3f8944800cc48e1cbc29a5ee12d8542d>. The authors would
745 like to thank Noel Keenlyside, Thomas Toniazzo and Yushi Morioka for their helpful
746 discussions.

747

748 **References**

749 AchutaRao K, Sperber KR (2006) ENSO simulation of coupled ocean-atmosphere models: are
750 the current models better? *Clim Dyn* 27:1–15

751 Allan RJ, Lindesay JA, Reason CJC (2003) Multidecadal variability in the climate system over
752 the Indian Ocean region during the austral summer. *J Clim* 8:185–1873.

753 Ault TR, Cole JE, St. George S (2012) The amplitude of decadal to multidecadal variability in
754 precipitation simulated by state-of-the-art climate models. *Geophys Res Lett* 39: L21705.
755 doi: 10.29/2012GL053424..

756 Ault TR, Deser C, Newman M, Emile-Geay J (2013) Characterizing decadal to centennial
757 variability in the equatorial Pacific during the last millennium. *Geophys Res Lett* 40:3450–
758 3456.

759 Ba J, Keenlyside N, Latif M, Park W, Ding H, Lohmann K, Mignot J, Menary M, Ottera O,
760 Wouters B, Salas y Melia D, Oka A, Belluci A, Volodin E (2014) A multi-model comparison
761 for Atlantic multidecadal variability. *Clim Dyn* 9:2333-2348.

762 Beraki AF, DeWitt DG, Landman WA, Olivier C (2014) Dynamical Seasonal Climate
763 Prediction Using an Ocean-Atmosphere Coupled Climate Model Developed in Partnership
764 between South Africa and the IRI. *J Clim* 27:1719–1741.

765 Capotondi A, Wittenberg A, Masina S (2006) Spatial and temporal structure of Tropical Pacific
766 interannual variability in 20th century coupled simulations. *Ocean Modelling* 15:274–278.

767 Ciasto LM, Alexander MA, Deser C, and England MH (2011) On the persistence of cold-season
768 SST anomalies associated with the Annular Mode. *J Clim* 24:2500–2515.

769 Compo GP, Whitaker JS, and Sardeshmukh PD (2006) Feasibility of a 100 year reanalysis using
770 only surface pressure data. *Bull Amer Met Soc* 87:175–190.

771 Compo GP, Whitaker JS, Sardeshmukh PD, Matsui N, Allan RJ, Yin X, Gleason BE, Vose
772 RS, Rutledge G, Bessemoulin P, Brönniman S, Brunet M, Crouthamel RI, Grant AN.,
773 Groisman PY, Jones JD, Kruk M, Kruger AC, Marshall GJ, Maugeri M, Mok HY, Nordli
774 Ø, Ross TF, Trigo RM, Wang XL, Woodruff SD, Worley SJ (2011) The twentieth century
775 reanalysis project. *Quarterly J Roy Meteorol Soc* 137:1–28.

776 Conway D (2015) Climate and southern Africa's water-energy-food nexus. *Nat Clim Change*
777 5:837–846.

778 Cook KH (2001) A Southern Hemisphere wave response to ENSO with implications for
779 southern Africa precipitation. *J Atmos Sci* 15:2146–2162.

780 Crétat J, Pohl B, Dieppois B, Berthou S, Pergaud J (2018) The Angola Low: relationship with
781 southern African rainfall and ENSO. *Climate Dynamics* Published online.
782 doi.org/10.1007/s00382-018-4222-3

783 Crétat J, Richard Y, Pohl B, Rouault M, Reason CJC, Fauchereau N (2012) Recurrent daily
784 rainfall patterns over South Africa and associated dynamics during the core of the austral
785 summer. *Int J Climatol* 32:261–273.

786 De Viron O, Dickey JO, Ghil M (2013) Global modes of variability. *Geophys Res Let* 40:1832–
787 1837.

788 Deser C, Phillips A, Bourdette V, Teng H (2012) Uncertainty in climate change projections:
789 the role of internal climate variability. *Clim Dyn* 38:527–546.

790 Dieppois B, Rouault M, New M (2015) The impact of ENSO on Southern African rainfall in
791 CMIP5 ocean atmosphere coupled climate models. *Clim Dyn* 45:2425–2442.

792 Dieppois B, Pohl B, Rouault M, New M, Lawler D, Keenlyside N (2016) Interannual to
793 interdecadal variability of winter and summer southern African rainfall, and their
794 teleconnections. *J Geophys Res-Atmos* 121: 6215–6239

795 Di Lorenzo E, Liguori G, Schneider N, Furtado JC, Anderson BT, Alexander MA (2015) ENSO
796 and meridional models: A null hypothesis for Pacific climate variability. *Geophys Res Let*
797 42:9440–9448.

798 Fauchereau N, Trzaska S, Richard Y, Roucou P, Camberlin P (2003) Sea-surface temperature
799 co-variability in the southern Atlantic and Indian Oceans and its connections with the
800 atmospheric circulation in the Southern Hemisphere. *Int J Clim* 23:663–677.

801 Fleming LE, Anchukaitis KJ (2016) North Pacific decadal variability in the CMIP5 last
802 millennium simulations. *Clim Dyn* 47:3783–3801.

803 Ghil M, Allen MR, Dettinger MD, Ide K, Kondrashov D, Mann ME, Robertson AW, Saunders
804 A, Tian Y, Varadi F, Yiou P (2002) Advanced spectral methods for climatic time series.
805 *Reviews of Geophysics* 40:3-1-3-41.

806 Guilyardi E, Wittenberg A, Fedorov A, Collins M, Wang C, Capotondi A, van Oldenborg GJ,
807 Stockdate T (2009) Understanding El Niño in Ocean-Atmosphere General Circulation
808 Models: Progress and Challenges. *Bull Amer Meteor Soc* 90:325–340.

809 Harris I, Jones PD, Osborn TJ, Lister DH (2014) Updated high-resolution grids of monthly
810 climatic observations - the CRU TS3.10 Dataset. *Int J Clim* 34:623–642.

811 Hart NCG, Reason CJC, Fauchereau N (2012) Cloud bands over southern Africa: seasonality,
812 contribution to rainfall variability and modulation by the MJO. *Clim Dyn* 41:119–1212.

813 Hawkins E, Sutton R (2009) The potential to Narrow Uncertainty in Regional Climate
814 Predictions. *Bull Amer Meteor Soc* 90:1095–1108.

815 Henley BJ, Meehl G, Power SB, Folland CK, King A, Brown JN, Karoly DJ, Delage F, Gallant
816 AJE, Freund M, Neukom R (2017) Spatial and temporal agreement in climate model
817 simulations of the Interdecadal Pacific Oscillation. *Environ Res Lett* 12:044011.

818 Hermes JC, Reason CJC (2005) Ocean Model Diagnosis of Interannual Coevolving SST
819 Variability in the South Indian and South Atlantic Oceans. *J Clim* 18:2864–2882.

820 Hewitson BC, Crane RG (2006) Consensus between GCM climate change projections with
821 empirical downscaling: precipitation downscaling over South Africa. *Int J Clim* 26:1315–
822 1337.

823 Hiraha S, Ishii M, Fukuda Y (2014) Centennial-scale sea surface temperature analysis and its
824 uncertainty. *J Clim* 27:57–75.

825 Hoell A, Funk C, Magadzire T, Zinke J, Husak G (2015) El Niño-Southern Oscillation diversity
826 and Southern Africa teleconnections during Austral Summer. *Clim Dyn* 45:1583–1599.

827 Hoell A, Funk C, Zinke J, Harrison L (2017) Modulation of the Southern Africa precipitation
828 response to the El Niño Southern Oscillation by the subtropical Indian Ocean Dipole. *Clim*
829 *Dyn* 48:2529–2540.

830 Hoell A, Cheng L (2018) Austral summer Southern Africa precipitation extremes forced by the
831 El Niño Southern Oscillation and the subtropical Indian Ocean Dipole. *Clim Dyn* 50:3219–
832 3236.

833 Hoskins BJ, Ambrizzi T (1993) Rossby Wave Propagation on a Realistic Longitudinally
834 Varying Flow. *J Atmos Sci* 50:1661–1671.

835 Huang B, Banzon VF, Freeman E, Lawrimore J, Liu W, Peterson TC, Smith TM, Thorne PW,
836 Woodruff SD, Zhang HM (2015) Extended Reconstructed Sea Surface Temperature Version
837 4 (ERSST.v4). Part I: Upgrades and Intercomparisons. *J Clim* 28:911–930.

838 Huang B, Thorne PW, Smith TM, Liu W, Lawrimore J, Banzon F, Zhang H-M, Peterson TC,
839 Menne M (2015) Further Exploring and Quantifying Uncertainties of Extended
840 Reconstructed Sea Surface Temperature (ERSST) Version 4 (v4). *J Clim* 29:3119–3142.

841 James R, Washington R, Abiodun B, Kay G, Mutemi J, Pokam W, Hart N, Artan G, Senior C
842 (2018) Evaluating climate models with an African lens. *Bull Amer Meteor Soc* 99:313–336.

843 Jun M, Knutti R, Nychka DW (2008) Local eigenvalue of CMIP3 climate model errors. *Tellus*
844 *A* 60:992–1000.

845 Kalogomou EA, Lennard C, Shongwe M, Pinto I, Favre A, Kent M, Hewitson B, Dosio A,
846 Nikulin G, Panitz H-J, Buchner M (2013) A Diagnostic Evaluation of Precipitation in
847 CORDEX Models over Southern Africa. *J Clim* 26:9477–9506.

848 Kane RP (2009) Periodicities, ENSO effects and trends of some South African rainfall series:
849 an update. *S Afr J Sci* 105:199–207.

850 Kay JE, Deser C, Phillips A, Mai A, Hannay C, Strand G, Arblaster JM, Bates SC, Danabasoglu
851 G, Edwards J, Holland M, Kushner P, Lamarque J, Lawrence D, Lindsay K, Middleton A,
852 Munoz E, Neale R, Oleson K, Polvani L, Vertenstein M (2015) The Community Earth
853 System Model (CESM) Large Ensemble Project: A Community Resource for Studying
854 Climate Change in the Presence of Internal Climate Variability. *Bull Amer Meteor Soc* 96:
855 1333–1349

856 Keenlyside NS, Latif M, Jungclauss J, Kornblueh L, Roeckner E (2008) Advancing decadal-
857 scale climate prediction in the North Atlantic sector. *Nature* 453:84–88.

858 Klein SA, Soden BJ, Lau NC (1999) Remote sea surface variations during ENSO: evidence
859 for a tropical atmospheric bridge. *J Clim* 12:917–932.

860 Knutti R. (2010) The end of model democracy? *Climatic Change* 102:395–404.

861 Knutti R, Meehl GA, Allen R, Stainforth DA (2006) Constraining climate sensitivity from the
862 seasonal cycle in surface temperature. *J Clim* 19:4224–4233.

863 Laepple T, Huybers P (2014) Ocean surface temperature variability: Large model-data
864 differences at decadal and longer periods. *Proc Natl Acad Sci* 111:16682–16687.

865 Landman WA, Beraki A (2012) Multi-model forecast skill for mid-summer rainfall over
866 southern Africa. *Int J Clim* 32:303–314.

867 Landman WA, Engelbrecht F, Hewitson B, Malherbe J, van der Merwe J (2017) Towards
868 bridging the gap between climate change projections and maize producers in South Africa.
869 *Theor Appl Climatol* 132:1153–1163.

870 Lazenby C, Todd M, Wang Y (2016) Climate model simulation of South Indian Ocean
871 Convergence Zone: Mean state and variability. *Clim Res* 68:59–71.

872 Lee T, Waliser DE, Li JL, Landerer FW, Gierach MM (2013) Evaluation of CMIP3 and CMIP5
873 Wind Stress Climatology Unising Satellite Measurements and Atmospheric Reanalysis
874 *Produc. J Clim* 26:5810–5826.

875 Lim E-P, Hendon HH, Arblastger JM, Delage F, Nguyen H, Min S-K, Wheeler MC (2016) The
876 impact of the Southern Annular Mode on Future changes in Southern Hemisphere rainfall.
877 *Geophys Res Lett* 43:7160–7167.

878 Lin J-L (2007) The Double ITCZ Problem in IPCC AR4 Couple GCMs: Ocean–Atmosphere
879 Feedback Analysis. *J Clim* 20:4497–4525.

880 Lindesay JA (1988) South African rainfall, the Southern Oscillation and a Southern Hemisphere
881 semi-annual cycle. *J Climatol* 8:17–30.

882 Lübbecke JF, Böning CW, Keenlyside NS, Xie S-P (2010) On the connection between
883 Benguela and equatorial Atlantic Niños and the role of the South Atlantic Anticyclone. *J*
884 *Geophys Res-Oceans* 115:C0915. doi:10.1029/2009JC005964.

885 Lyon B, Mason SJ (2007) The 1997-98 summer season in southern Africa. Part I: Observations.
886 *J Clim* 20:5134–5148.

887 Macron C, Pohl B, Richard Y, Bessafi M (2014) How do tropical-temperate troughs form and
888 develop over southern Africa? *J Clim* 27:1633–1647.

889 Malherbe J, Landman WA, Engelbrecht FA (2014) The bi-decadal rainfall cycle, Southern
890 Annular Mode and tropical cyclones over the Limpopo River Basin, southern Africa. *Clim*
891 *Dyn* 42:3121–3138.

892 Malherbe J, Dieppois B, Maluleke P, Van Staden M, Pillay DL(2016) South African droughts
893 and decadal variability. *Nat. Hazards* 80:657–681.

894 Mann ME, Park J (1994) Global modes of surface temperature variability on interannual to
895 century timescales. *J Geophys Res-Atmos* 99:25819–25833.

896 Mantua NJ, Hare SR (2002) The Pacific Decadal Oscillation. *J Oceanogr* 58:35–44.

897 Mantua NJ, Hare SR, Zhang Y, Wallace JM, Francis RC (1997), A Pacific Interdecadal Climate
898 Oscillation with Impacts on Salmon Production. *Bull Amer Meteor Soc* 78:1069–1079.

899 Mason SJ (1998) Seasonal forecasting of South Africa rainfall using a non-linear discriminant
900 analysis model. *Int J Clim* 18:147–164.

901 Mason SJ, Jury M (1997) Climatic variability and change over the Southern Africa: a reflection
902 on underlying processes. *Prog Phys Geo* 21:23–50.

903 Menary MB, Hodson DLR, Robson JI, Sutton RT, Wood RA, Hunt JA (2015) Exploring the
904 impact of CMIP5 model biases on the simulation of North Atlantic decadal variability.
905 *Geophys Res Lett* 42:5926–5934.

906 Morioka Y, Engelbrecht F, Behera S (2015) Potential sources of multidecadal climate
907 variability over southern Africa. *J Clim* 28:8695–8709.

908 Munday C, Washington R (2016) Circulation controls on southern African precipitation in
909 coupled models: The role of the Angola Low. *J Geophys Res-Atmos* 122:861–877.

910 Munday C, Washington R (2018) Systematic Climate Model Rainfall Biases over Southern
911 Africa: Links to Moisture Circulation and Topography. *J Clim* 31:7533–7548.

912 Newman M, Alexander MA, Ault T, Cobb KM, Deser C, Di Lorenzo E, Mantua NJ, Miller AJ,
913 Minobe S, Nakamura H, Schneider N, Vimont DJ, Phillips AS, Scott JD, Smith CA (2016)
914 The Pacific Decadal Oscillation, Revisited. *J Clim* 29:4399–4427.

915 Nicholson SE, Kim J (1997) The relationship of the El Niño-Southern Oscillation to African
916 rainfall. *Int J Clim* 17:117–135.

917 Nikulin G, Jones C, Giorgi F, Asrar G, Buchner M, Cerezo-Mota R, Christensen OB, Déqué
918 M, Fernandez J, Hansler A, van Meijgaard E, Samuelsson P, Sylla MB, Sushama L (2012)
919 Precipitation Climatology in an Ensemble of CORDEX-Africa Regional Climate
920 Simulations. *J Clim* 25:6057–6078.

921 Pohl B, Dieppois B, Crétat J, Lawler DM, Rouault M (2018) From synoptic to interdecadal
922 variability in southern African rainfall: towards a unified view across timescales. *J Clim*
923 31:5845–5872.

924 Power S, Casey T, Folland CK, Colman A, Mehta V (1999) Inter-decadal modulation of the
925 impact of ENSO on Australia. *Clim Dyn* 15:319–323.

926 Power S, Delage F, Wang G, Smith I, Kociuba G (2017) Apparent limitations in the ability of
927 CMIP5 climate models to simulate recent multi-decadal change in surface temperature:
928 implications for global temperature projections. *Clim Dyn* 49:53–69.

929 Ratnam JV, Behera SK, Masumoto Y, Yamagata T (2014) Remote effects of El Niño and
930 Modoki events on the Austral Summer Precipitation of Southern Africa. *J Clim* 27:3802–
931 3815.

932 Rayner NA, Parker DE, Horton EB, Folland CK, Alexander LV, Rowell DP, Kent EC, Kaplan
933 A (2003) Global analyses of sea surface temperature, sea ice, and night marine air
934 temperature since the late nineteenth century. *J Geophys Res-Atmos* 108:4407.
935 doi:10.1029/2002JD002670

936 Reason CJC (1998) Warm and cold events in the southeast Atlantic/southwest Indian Ocean
937 region and potential impacts on circulation and rainfall over southern Africa. *Meteorog*
938 *Atmos Phys* 69:49–65.

939 Reason CJC (2001) Subtropical Indian Ocean SST dipole events and southern African rainfall.
940 *Geophys Res Lett* 28:2225–2227.

941 Reason CJC, Mulenga H (1999) Relationships between South African rainfall and SST
942 anomalies in the southwest Indian Ocean. *Int J Climatol* 19:1651–1673.

943 Reason CJC, Smart S (2015) Tropical south east Atlantic warm events and associated rainfall
944 anomalies over southern Africa. *Front Environ Sci* 3:1-11. doi:10.3389/fenvs.2015.00024

945 Reynolds RW, Rayner NA, Smith TM, Stokes DC, Wang W (2002) An improved in situ and
946 satellite SST analysis for climate. *J. Clim.*, **15**, 1609–1625.

947 Richard Y, Fauchereau N, Poccard I, Rouault M, Trzaska S (2001) XXth century droughts in
948 Southern Africa: spatial and temporal variability, teleconnections with oceanic and
949 atmospheric conditions. *Int. J. Clim.*, **21**, 873–885.

950 Ropelewski CF, Halpert MS (1987) Global and regional scale precipitation patterns associated
951 with the El Niño/Southern Oscillation. *Mon Wea Rev* 115:1606–1626.

952 Ropelewski CF, Halpert MS (1989) Precipitation patterns associated with the high indices
953 phase of the southern oscillation. *J Clim* 2:268–284.

954 Rouault M (2012) Bi-annual intrusion of tropical water in the northern Benguela upwelling.
955 *Geophys Res Lett* 39:L12606. doi:10.1029/2012GL052099

956 Rouault M, Richard Y (2005) Intensity and spatial extent of droughts in Southern Africa.
957 *Geophys Res Lett* 32:L15702. doi:10.1029/2005GL022436.

958 Sarachick ES, Cane MA (2010) *The El Niño-Southern Oscillation Phenomenon*. Cambridge
959 University Press, Cambridge.

960 Schneider N, Cornuelle BD (2005) The forcing of the Pacific Decadal Oscillation. *J Clim*
961 18:4355–4373.

962 Schneider U, Becker A, Finger P, Meyer-Christoffer A, Ziese M, Rudolf B (2014) GPCP's new
963 land surface precipitation climatology based on quality controlled in situ data and its role in
964 quantifying the global water cycle. *Theor Appl Climatol* 115:15–40.

965 Shimodaira H (2002) An approximately unbiased tests of phylogenetic tree selection.
966 *Systematic Biology* 51:492–508.

967 Shimodaira H (2004) Approximately unbiased tests of regions using multistep-multiscale
968 bootstrap resampling. *Annals of Statistics* 32:2616–2641.

969 Taylor KE, Stouffler RJ, Meehl GA (2012) An overview of CMIP5 and the experiment design.
970 *Bull Am Meteorol Soc* 93:485–498.

971 Todd MC, Washington R (1999) Circulation anomalies associated with tropical-temperate
972 troughs in southern Africa and the southwest Indian Ocean. *Clim Dyn* 15:937–951.

973 Tourre YM, Cibot C, Terray L, White WB, Dewitte B (2005) Quasi-decadal and inter-decadal
974 climate fluctuations in the Pacific Ocean from a CGCM. *Geophys Res Lett* 32:L07710.
975 doi:10.1029/2004GL022087

976 Tourre YM, Kushnir Y, White WB (1999) Evolution of interdecadal variability in sea level
977 pressure, sea surface temperature, and upper ocean temperature over the Pacific Ocean. *J*
978 *Phys Oceanogr* 9:1528–1541.

979 Tourre YM, Rajagopalan B, Kushnir Y, Barlow M, White WB (2001) Patterns of coherent
980 ocean decadal and interdecadal climate signals in the Pacific basin during the 20th century.
981 *Geophys Res Lett* 28:2069–2072.

982 Trenberth K (1997) The Definition of El Niño. *Bull Am Meteorol Soc* 78:2771–2778.

983 Tyson PD (1981) Atmospheric circulation variations and the occurrence of extended wet and
984 dry spells over southern Africa. *J Climatol* 1:115–130.

985 Tyson PD (1986) *Climatic Change and variability over southern Africa*. Oxford University
986 Press, Cape Town.

987 Venegas S, Mysak LA, Straub DN (1997) Atmosphere-ocean coupled variability in the South
988 Atlantic. *J Clim* 10:2904–2920.

989 Vigaud N, Richard Y, Rouault M, Fauchereau N (2009) Moisture transport between the South
990 Atlantic Ocean and southern Africa: relationships with summer rainfall and associated
991 dynamics. *Clim Dyn* 32:113–123.

992 Ward JH (1963) Hierarchical Grouping to Optimize an Objective Function. *Journal of the*
993 *American Statistical Association* 58:236–244.

994 Washington R, Preston A (2006) Extreme wet years over southern Africa: Role of Indian Ocean
995 sea surface temperatures. *J Geophys Res-Atmos* 111:D15104. doi:10.1029/2005JD006724

996 Wu Z, Huang NE, Long SR, Peng C-K (2007) On the trend, detrending, and variability of
997 nonlinear and nonstationary time series. *Proc Natl Acad Sci USA* 104:14889–14894.
998 Yue S, Wang C (2004) The Mann-Kendall test modified by effective sample size to detect trend
999 in serially correlated hydrological series. *Water Resources Management* 18:201–218.
1000 Zhang Q, Kornich H, Holmgren K (2013) How well do reanalyses represent the southern
1001 African precipitation. *Clim Dyn* 40:951–962.

1002

1003

1004

1005

1006

1007

1008

1009

1010

1011

1012

1013

1014

1015

1016

1017

1018

1019

1020

Figures and Captions

1021
1022
1023
1024
1025
1026
1027
1028
1029
1030
1031
1032
1033
1034
1035
1036
1037
1038
1039
1040
1041
1042
1043
1044

Table 1 Summarized information on observation data and CMIP5 models used in the study.

Table 2 Different components of CMIP5 CGCMs used in the study. Shades of orange, blue, green and grey indicate shared components between CGCMs from different institutions.

Fig. 1 Summer (NDJF) differences between simulated and observed SA rainfall fields. **a** Multimodel mean of 95 historical runs from 28 CMIP5 models of summer-rainfall average minus the CRU TS 3.24.01 observations, compared to the NDJF rainfall climatology (*black dashed contours*), between 1901 and 2005. Statistical significance of differences in mean (*white colours*) has been estimated using a Student *t*-test at $p = 0.05$. **b** CMIP5 Multimodel agreement in the difference in summer-rainfall average compared with observation **c** Spatial distribution of the summer-rainfall region in the CMIP5 models (*coloured contours refer to each individual model; cf. Table 1*) and in the CRU TS 3.24.01 observations (*grey shaded*). **d** Multimodel agreement in the location of the summer-rainfall region in the CMIP5 models compared to observation (*grey contour*). The summer-rainfall region, which is used to calculate the SRI, has been defined as the area in which the wettest month of the year occur between November and February on average between 1901 (1850/60) and 2005 in the observations (CMIP5 models).

1045 **Fig. 2** Timescales of variability in the simulated and observed SRI. **a** Comparison between FFT
1046 spectra from observation (CRU TS 3.24.01: 1901–2005) and 95 historical runs from 28 CMIP5
1047 models (1850/60–2005). *Bold contour lines* show the probability limits at $p = 0.05$ based on
1048 1000 Monte Carlo simulations of the red noise background spectrum. White crosses indicate
1049 area where FFT power spectral density could have been influenced by the sampling period. **b**
1050 Centred Ratio of standard deviation (1-rSD), here expressed in percentage, between simulations
1051 and observation according to the three dominant time-scales of variability. *Bold contour lines*
1052 indicates CMIP5 models simulating significantly equal SRI variance than observations at $p =$
1053 0.05 according to the Fisher's F -test. Summary of the mean biases per timescales is provided
1054 on the bottom left corner (*all model simulations: black; model simulation overestimating*
1055 *[underestimating] interannual variability: blue [red]*).

1056

1057 **Fig. 3** Summary of observed summer (NDJF) SA rainfall variability and its teleconnection with
1058 global SSTs at three different timescales. **a** Spatial patterns of rainfall standard deviations in
1059 observations (CRU TS 3.24.01). **b** Observed spatial patterns of global SST standard deviations
1060 (ERSSTv.4). *Bold red contour lines* delineates area where observed interannual to IDV variance
1061 are significantly greater than the red noise background spectrum at $p = 0.05$ based on 1000
1062 Monte Carlo simulations. **c** Observed global SST composite anomalies (ERSSTv.4) during
1063 enhanced SRI fluctuations (± 1 SD: wet years minus dry years) at the three different timescales.
1064 Statistical significance (*contours*) has been estimated by testing the difference in mean between
1065 SST anomalies during periods of rainfall variability greater and lower than 1 SD, through a
1066 modified t -test accounting for pseudoreplication in the series at $p = 0.05$. Displayed composite
1067 SST anomalies refer to wet conditions in SA, but are strictly opposite during dry conditions (cf.
1068 Fig. A1).

1069

1070 **Fig. 4** Evaluation of model performance and their diversity in simulating SA rainfall variance
1071 at three different timescales. **a-c** Taylor diagram of summer (NDJF) rainfall variance spatial
1072 patterns of 95 historical runs from 28 CMIP5 models (*coloured dot referring to each individual*
1073 *model; cf. Table 1*) and from observations (CRU TS 3.24.01; *grey dot*) at the IDV to interannual
1074 timescales. The diagram is a function of the root mean square (RMS, *green dashed circles–x-*
1075 *axis*), the correlation coefficient (*black dashed lines–y-axis*) and the SD (*blue dashed compared*
1076 *to solid circles–x-axis*). Since the values are normalized the reference (observation values) has
1077 a SD of 1. **d** Cluster diversity as determined using AHC, and in assessing significance of each
1078 cluster using multiscale bootstrapping. Colours indicate different clusters, and non-significantly
1079 clustered simulations are in white. Simulated rainfall fields have been remapped on a regular
1080 $0.5^{\circ} \times 0.5^{\circ}$ resolution grid to be compared to observation.

1081
1082 **Fig. 5** Summer-rainfall variance over SA at three different timescales in CMIP5 models. **a-c**
1083 Spatial patterns of rainfall standard deviations in six selected clusters from full CMIP5
1084 multimodel ensemble at the interannual to IDV timescales. *Dark red to dark blue contours lines*
1085 *on the bottom panels* delineates areas where IDV to interannual variance are significantly
1086 different than in observations at $p = 0.05$ according to the Fisher's F -test. The selected six
1087 clusters are ranked according to their variance (var), here expressed as the percentage of
1088 simulations in each cluster. Spatial correlations (cor[obs.]) between simulated and observed
1089 patterns are displayed for information purpose. *Asterisks* indicate significant Pearson's
1090 correlations at $p = 0.05$ between the cluster and the observed pattern. Note that QDV and IDV
1091 standard deviations have been multiplied by 2 for illustrative purpose. Simulated rainfall fields
1092 have been remapped on a regular $0.5^{\circ} \times 0.5^{\circ}$ resolution grid to be compared to observation.

1093

1094 **Fig. 6** Evaluation of model performance and their diversity in simulating NDJF SST variance
1095 and global SST composite anomalies at three different timescales. **a** Taylor diagram of NDJF
1096 SST variance spatial patterns of 95 historical runs from 28 CMIP5 models (*coloured dot*
1097 *referring to each individual model; cf. Table 1*) and from observations (ERSSTv.4; *grey dot*) at
1098 the IDV to interannual timescales. **b** as for **a** but for SST composite anomalies during enhanced
1099 SRI (± 1 SD: wet years minus dry years). **c** Cluster diversity for global SST variance and
1100 composite anomalies as determined using AHC, and in assessing significance of each cluster
1101 using multiscale bootstrapping. Colours indicate different clusters, and non-significantly
1102 clustered simulations are in white.

1103

1104 **Fig. 7** NDJF global SST variance at three different timescales in CMIP5 models. **a-c** Spatial
1105 patterns of global SST standard deviations in six selected clusters from full CMIP5 multimodel
1106 ensemble at the interannual to IDV timescales. *Dark red to dark blue contours lines* delineates
1107 areas where SST variance are significantly different than in observations at $p = 0.05$ according
1108 to the Fisher's F -test. The selected six clusters are ranked according to their variance (var), here
1109 expressed as the percentage of simulations in each cluster. Spatial correlations (cor[obs.])
1110 between simulated and observed patterns are displayed for information purpose. *Asterisks*
1111 indicate significant Pearson's correlations at $p = 0.05$ between clusters and the observed pattern.

1112

1113

1114

1115

1116

1117

1118

1119 **Fig. 8** as **Fig. 7** but for global SST composite anomalies in the CMIP5 models. *Black and grey*
1120 *contours* indicate that statistical significance of composite anomalies was reached in 50% of
1121 the model defining the cluster. Composite anomalies and statistical significances have been
1122 estimated as defined in Figure 3. The selected six clusters are ranked according to their variance
1123 (var), here expressed as the percentage of simulations in each cluster. Spatial correlations
1124 (cor[obs.]) between simulated and observed patterns are displayed for information purpose.
1125 *Asterisks* indicate significant Pearson's correlations at $p = 0.05$ between clusters and the
1126 observed pattern.

1127

1128 **Fig. 9** Comparison of performances in simulating SRI variability and associated SST
1129 teleconnections in the different ocean basins. Percentage of CMIP5 simulations associated with
1130 contrasted performances in SST variability and associated teleconnections has been quantified.
1131 +SST/+SRI refers to simulations with good SRI variability (*i.e.* significantly equal variance
1132 according to a Fisher F-test at $p = 0.05$) and good SST teleconnection patterns (*i.e.* Person
1133 correlations with observation ≥ 0.5). OppSST indicates simulations with good SRI variability,
1134 but opposite SST teleconnection patterns (*i.e.* Person correlation with observation < 0). +SST/-
1135 SRI refers to simulations with poor SRI variability (*i.e.* not significantly equal variance
1136 according to a Fisher F-test at $p = 0.05$), but with good SST teleconnection patterns. -SST/+SRI
1137 denotes simulations with good SRI variability, but with poor SST teleconnection patterns (*i.e.*
1138 Person correlations with observation < 0.5).

1139

1140

1141

1142

1143 **Fig. 10** Sample size uncertainties and model capabilities at the three different timescales. **a**
1144 Capability to simulate observed SRI variance (significant equal variance according to a Fisher
1145 F-test at $p = 0.05$) in all historical runs from the 28 CMIP5 models (*top*), and in their associated
1146 pi-Control runs (*bottom*). **b** Capability to simulate similar teleconnections (*i.e.* Pearson
1147 correlations ≥ 0.5) in all historical runs from the 28 CMIP5 models (*top*), and in their associated
1148 pi-Control runs (*bottom*). Grey dot sizes refer to the number of samples used to estimate the
1149 model capabilities, and should be used as an indicator of robustness.

1150

1151 **Fig. 11** Atmospheric bridges between the Pacific Ocean and SA in 20CR.v2c. NDJF velocity
1152 potential (ϕ ; *shaded*) and stream function (ψ ; *contours*) composite anomalies between 850 and
1153 600 hPa (*left*), and between 400 and 150 hPa (*right*), during enhanced SRI fluctuations (± 1 SD:
1154 wet years minus dry years) at the three different timescales. Composite anomalies and statistical
1155 significances have been estimated as defined in Figure 3. Only significant velocity potential
1156 and stream function anomalies at $p = 0.05$ are displayed. Note: IDV anomalies are multiplied
1157 by 1.5 to be clearly displayed.

1158

1159 **Fig. 12** Atmospheric bridges between the Pacific Ocean and SA in selected CMIP5 models. **a-**
1160 **c** Simulated NDJF velocity potential (ϕ ; *shaded*) and stream function (ψ ; *contours*) composite
1161 anomalies between 850 and 600 hPa during enhanced SRI fluctuations (± 1 SD: wet years minus
1162 dry years) at the three different timescales. Composite anomalies and statistical significances
1163 have been estimated as defined in Figure 3. Only significant velocity potential and stream
1164 function anomalies at $p = 0.05$ are displayed. Note: IDV anomalies are multiplied by 1.5 to be
1165 clearly displayed.

1166

1167 **Fig. A1** Comparison between SST composite anomalies associated with wet and dry conditions
1168 in SA. **a-c** Scatterplot of observed SST composite anomalies during wet (positive SRI
1169 anomalies = +1 SD) and dry (negative SRI anomalies = -1 SD) conditions at the interannual
1170 (*left*), QDV (*middle*) and IDV (*right*) timescales. **d-f** as **a-c** but for 95 historical runs from 28
1171 CMIP5 models. Scatter plots are smoothed and coloured (*low to high probability = blue, yellow*
1172 *to red*) using a 2D kernel density estimate. Red and black lines refer to the regression lines
1173 between wet and dry SST composite anomalies, and associated correlation coefficients are
1174 provided in the lower left corner on each panel.

1175

1176 **Fig. A2** Step-by-step process of the multi-scale bootstrap clustering. Step-0: 10 simulated
1177 patterns of global SST variability are submitted to the clustering approach. Step-1: simulated
1178 patterns are resampled n_i times, using r_j scales (referring to different sizes of the spatial
1179 domain). Step-2: $n_i \times r_j$ Agglomerative hierarchical clustering are produced, using Ward's
1180 agglomerative criteria applied to Euclidian distances. Step-3: the probability of each
1181 simulations to be clustered with the others (red values) is estimated. Here, only two clusters are
1182 significantly robust at $p \geq 0.90$.

1183

1184 **Fig. A3** Percentage of occurrence of significant signals within the interannual, QDV and IDV
1185 timescales of SRI variability in all (95) model simulations, in all (28) models and all (16)
1186 institutions using the CMIP5 historical experiments. Statistical significance was estimated at
1187 $p=0.05$ based 1000 Monte Carlo simulations of the red noise background spectrum.

1188

1189 **Fig. A4** Boxplots of the correlations between simulations of the same models (intra-ensembles;
1190 blue), and of different models (inter-models; red), of the CMIP5 historical experiments in
1191 reproducing spatial patterns of SA rainfall variability at the three different timescales.

1192

1193 **Fig. A5** Distributions of model simulations in clustering patterns of SA rainfall variability,
1194 global SST variability, and teleconnections at the interannual to interdecadal timescales. The
1195 six selected clusters, which are shown in Figures 5, 7 and 8, are in bold.

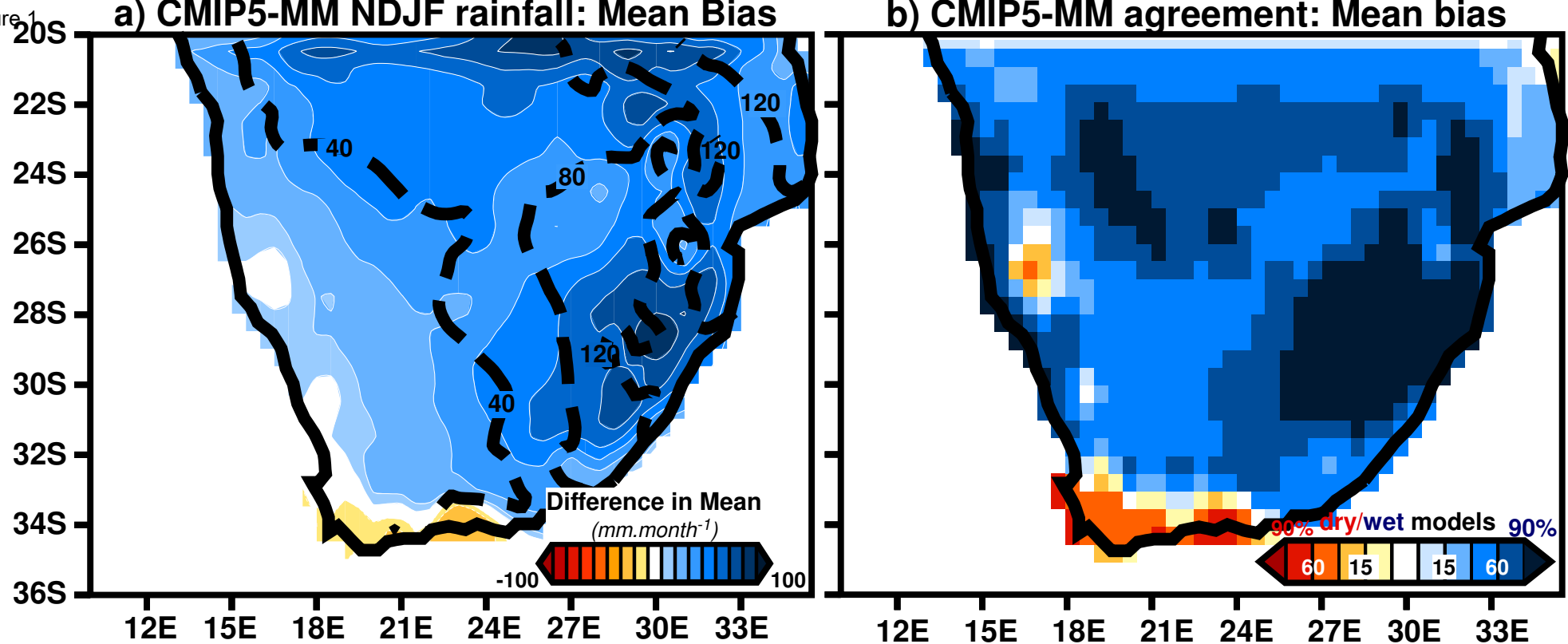
1196

1197 **Fig. A6** Boxplots of the correlations between simulations of the same models (intra-ensembles;
1198 blue), and of different models (inter-models; red), of the CMIP5 historical experiments in
1199 reproducing spatial patterns of global SST variability (shaded), and SST composite anomalies
1200 associated with SA rainfall variability (not shaded) at the three different timescales.

1201

1202 **Fig. A7** Mean annual cycle of monthly standard deviations of SST anomalies over the Niño3.4
1203 region (*i.e.* 5°S-5°N and 120-170°W) in the CMIP5 models (*coloured contours refer to each*
1204 *individual model; cf. Table 1*) and in the CRU TS 3.24.01 observations (*grey shaded*). SST
1205 anomalies are here calculated by subtracting the monthly climatology according to the
1206 definition of the Niño3.4 index (Trenberth 1997). To reduce the influence of the global trends,
1207 SST anomalies are detrended using a locally weighted linear regressions, with span equal to the
1208 length of the data.

Figure 1



c) CMIP5-MM agreement: Summer-rain Region

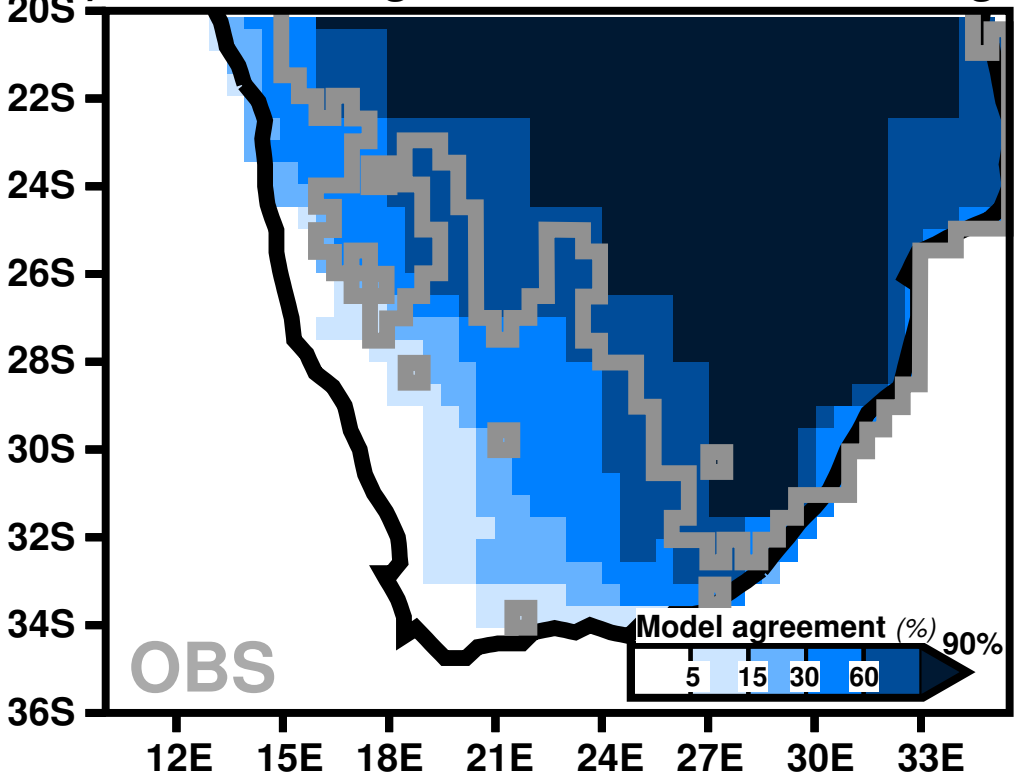


Figure 2

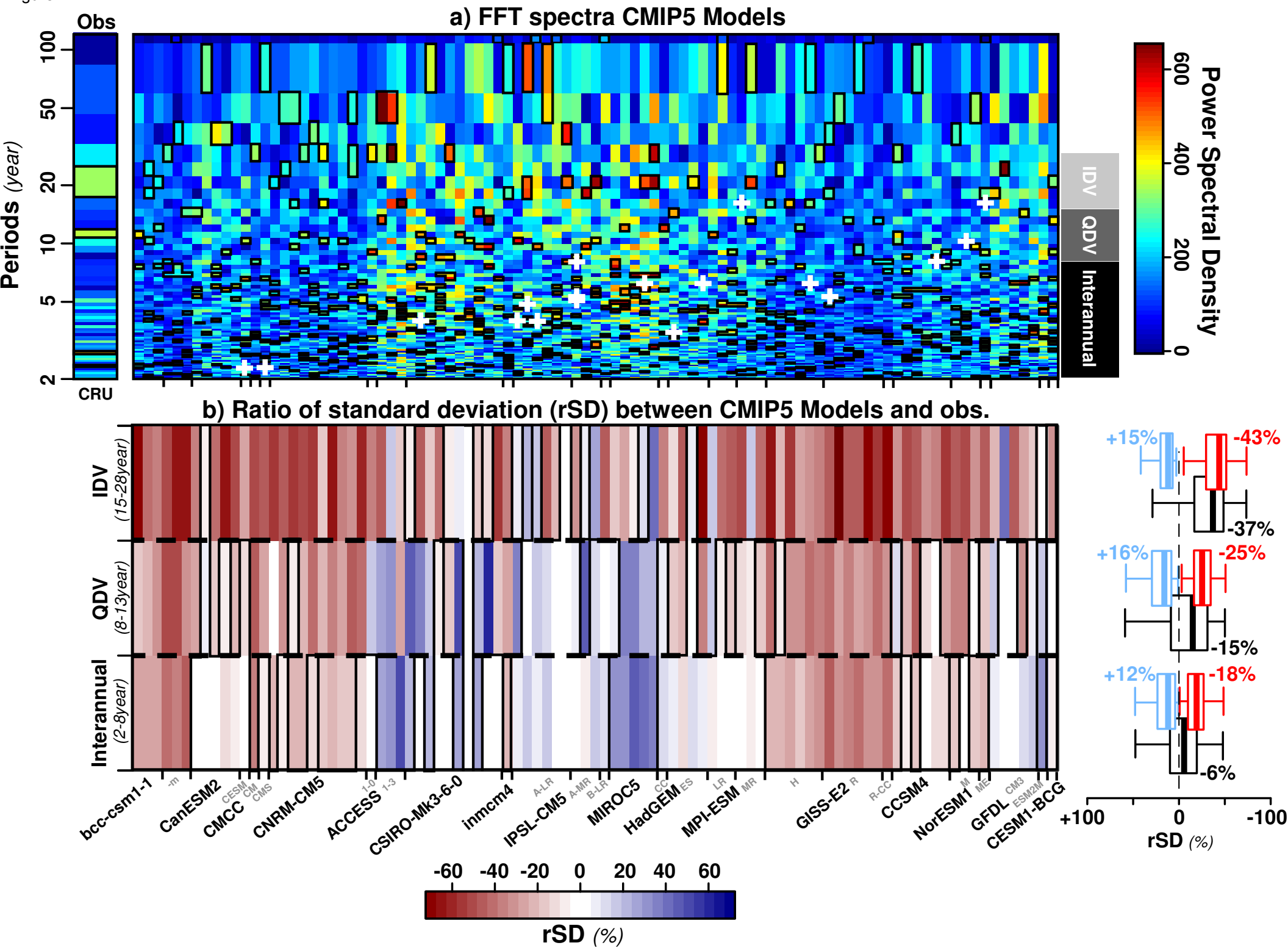
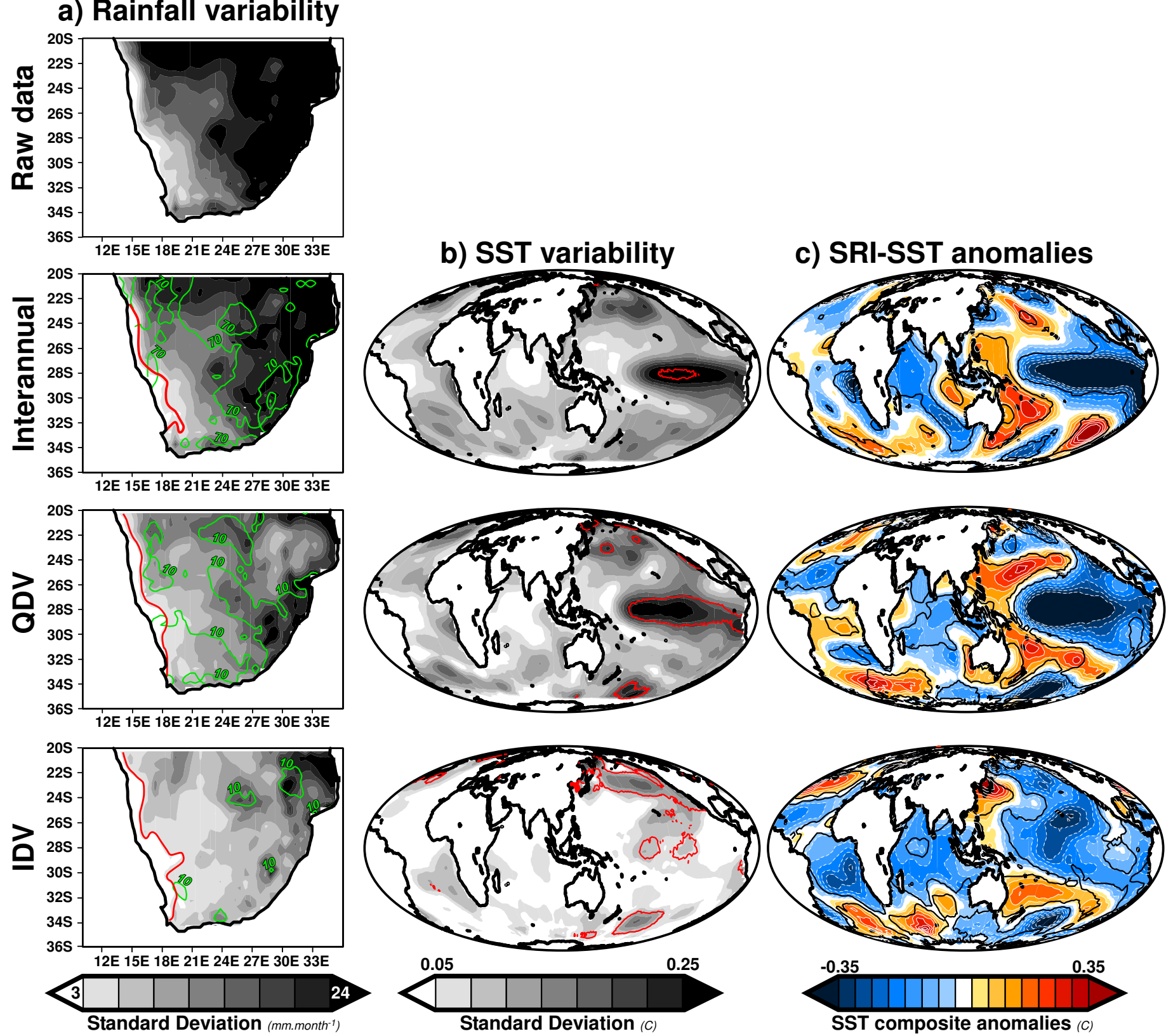


Figure 3



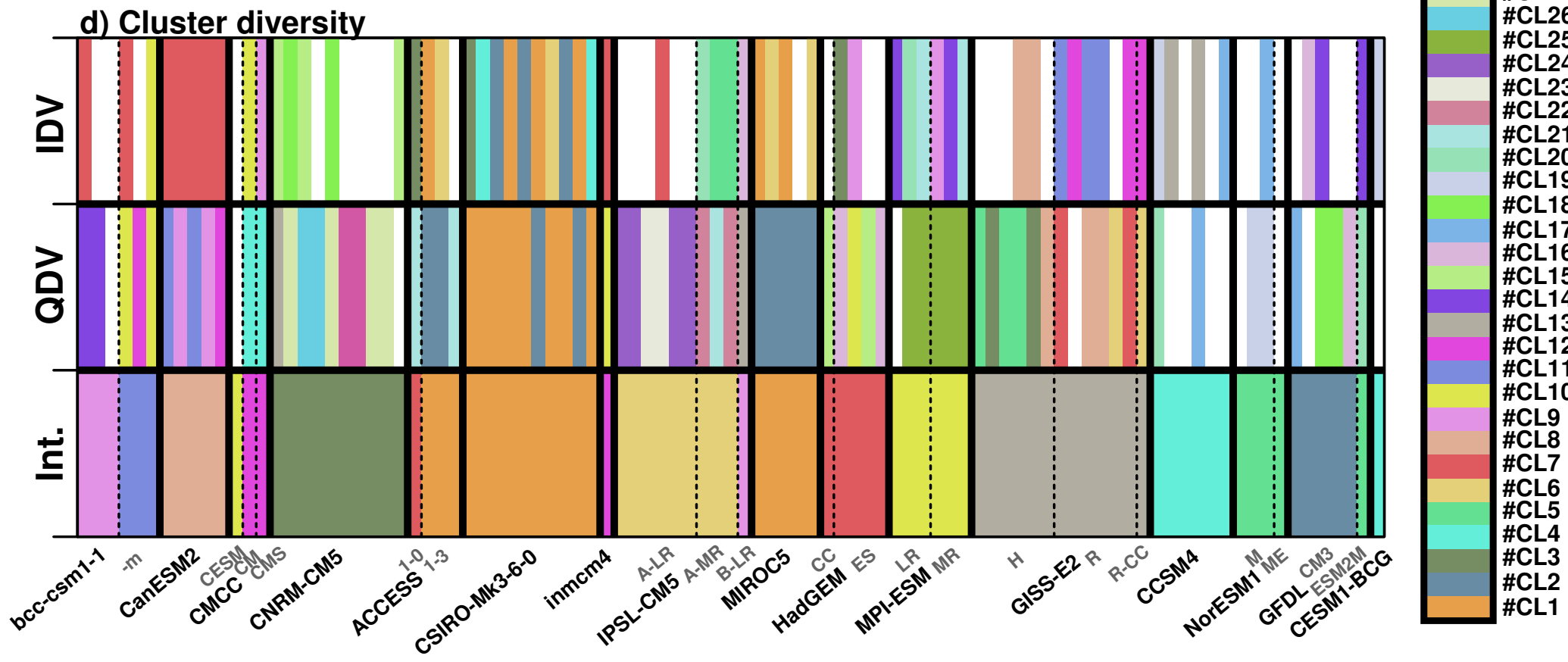
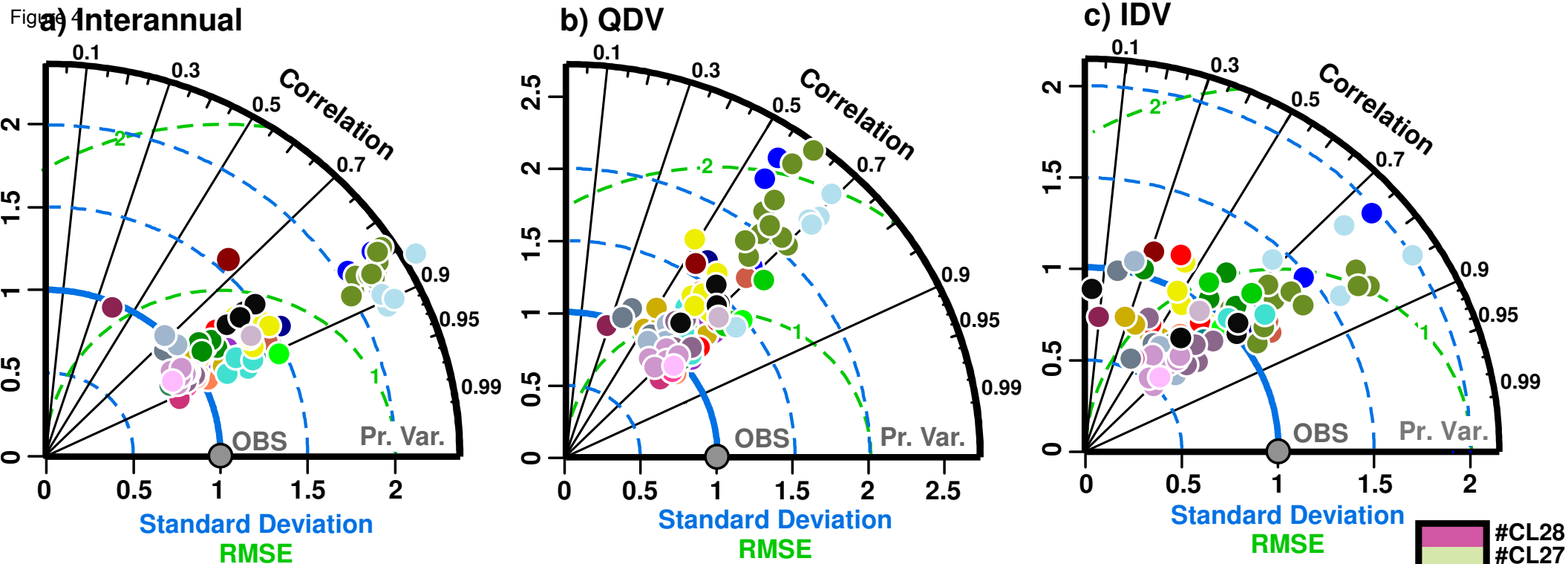


Figure 5

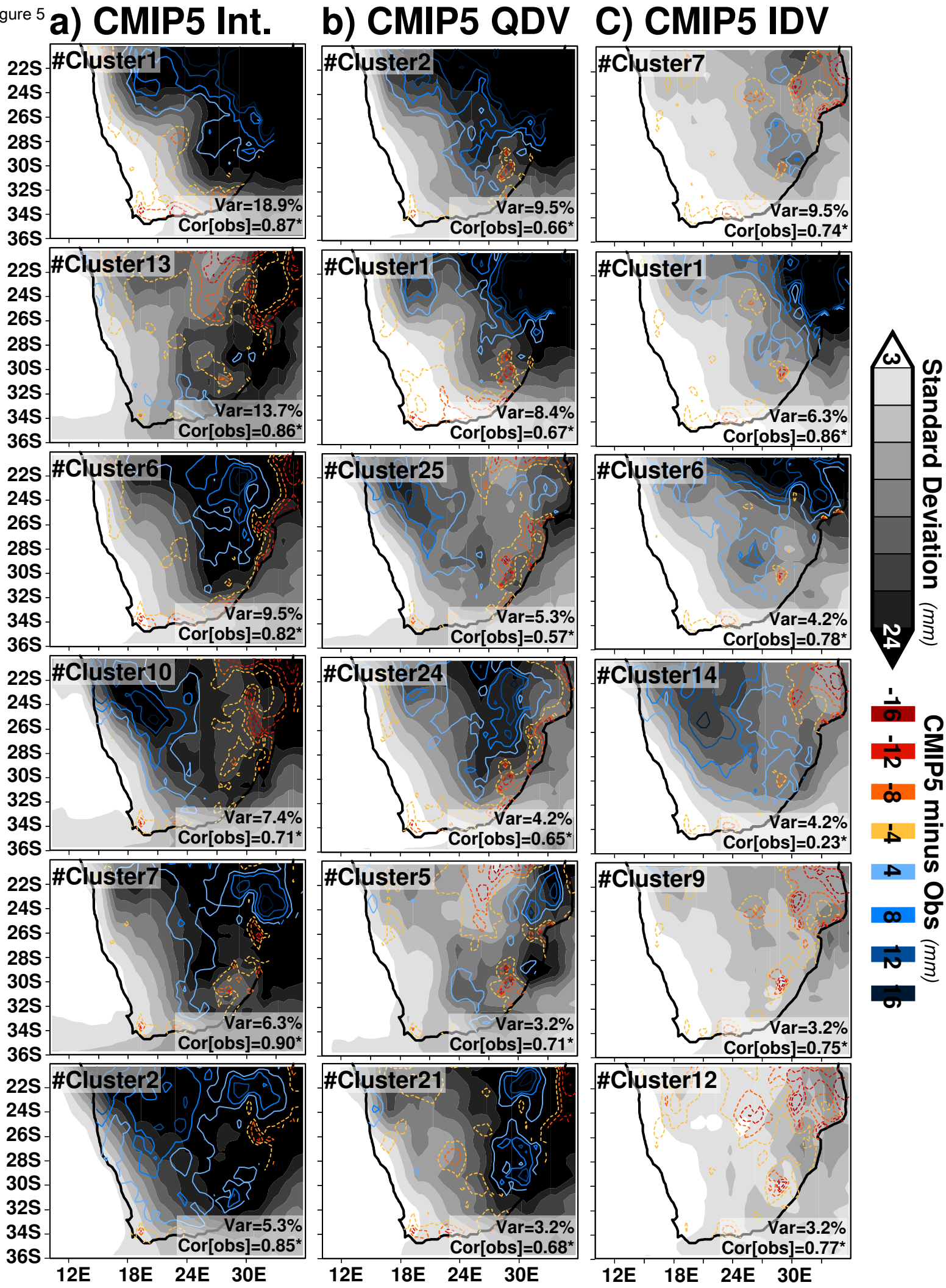


Figure 6

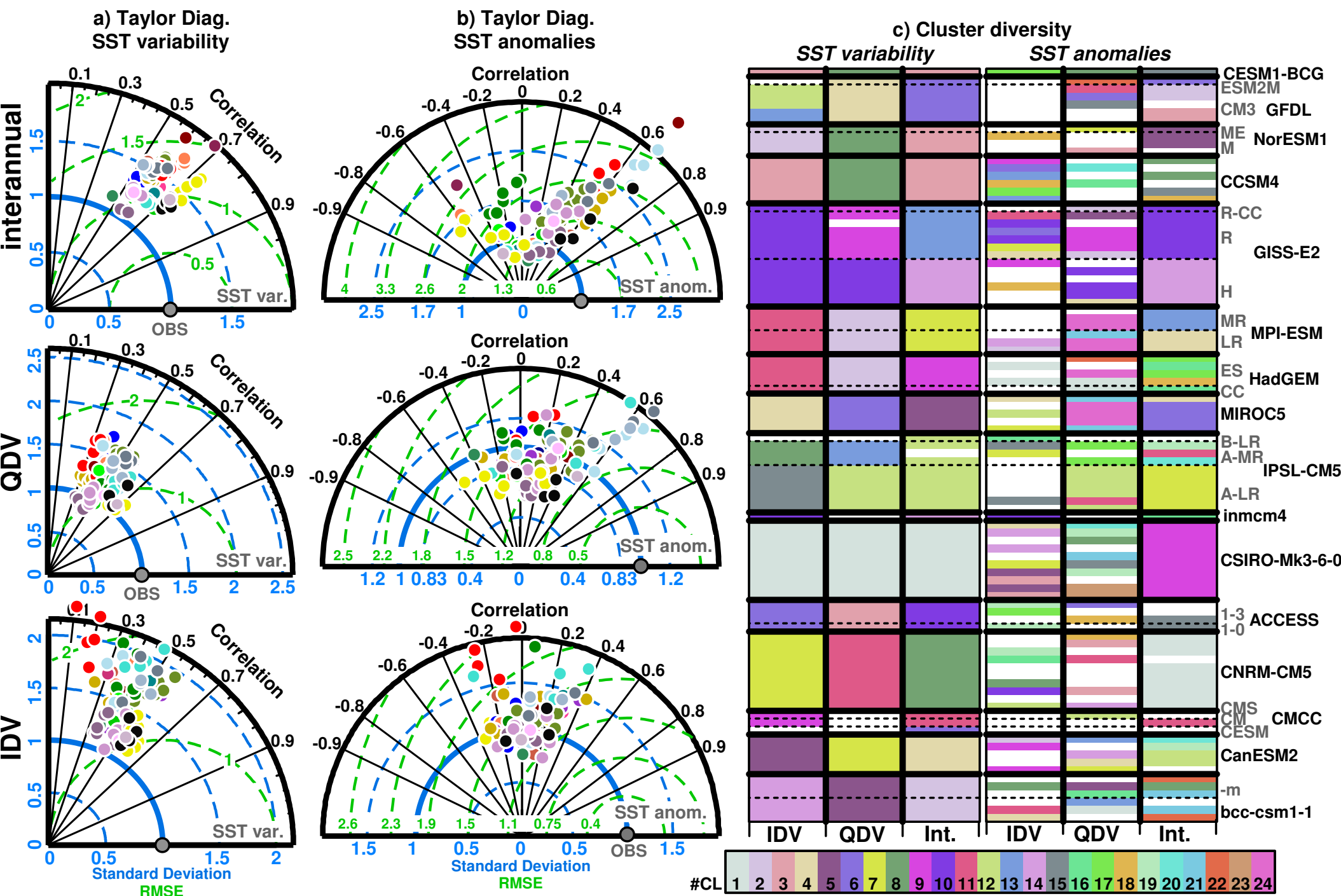


Figure 7

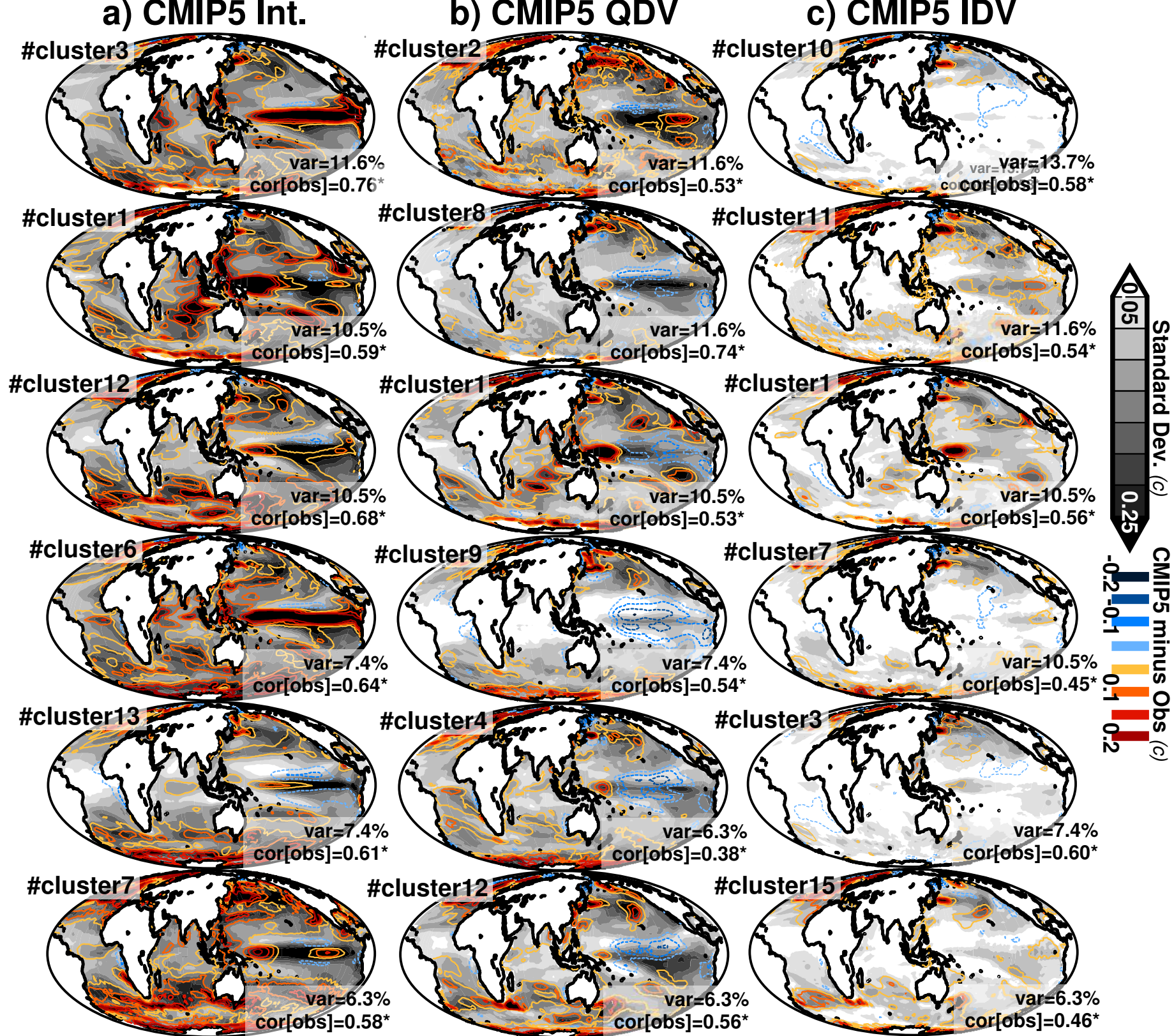


Figure 8

a) CMIP5 Int. Ano.

b) CMIP5 QDV Ano.

c) CMIP5 IDV Ano.

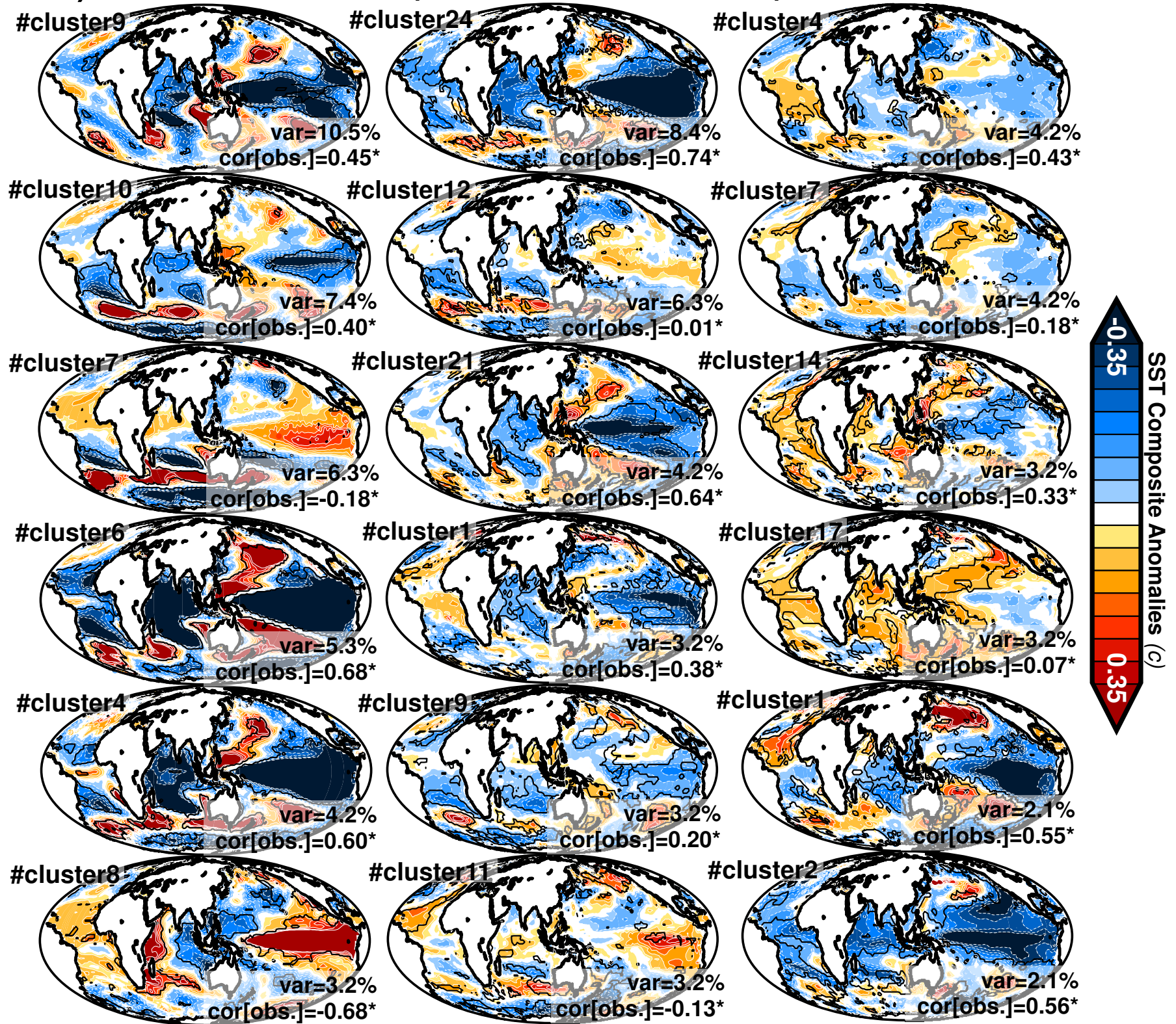


Figure 9

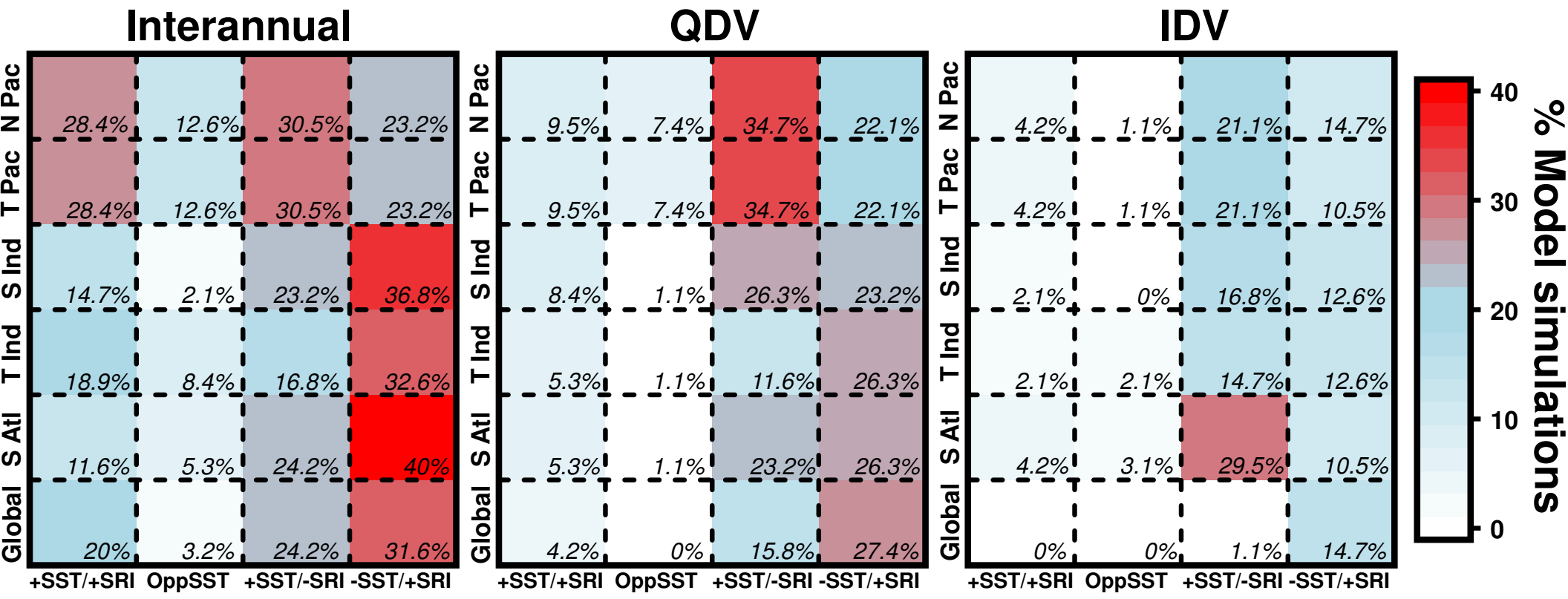


Figure 10

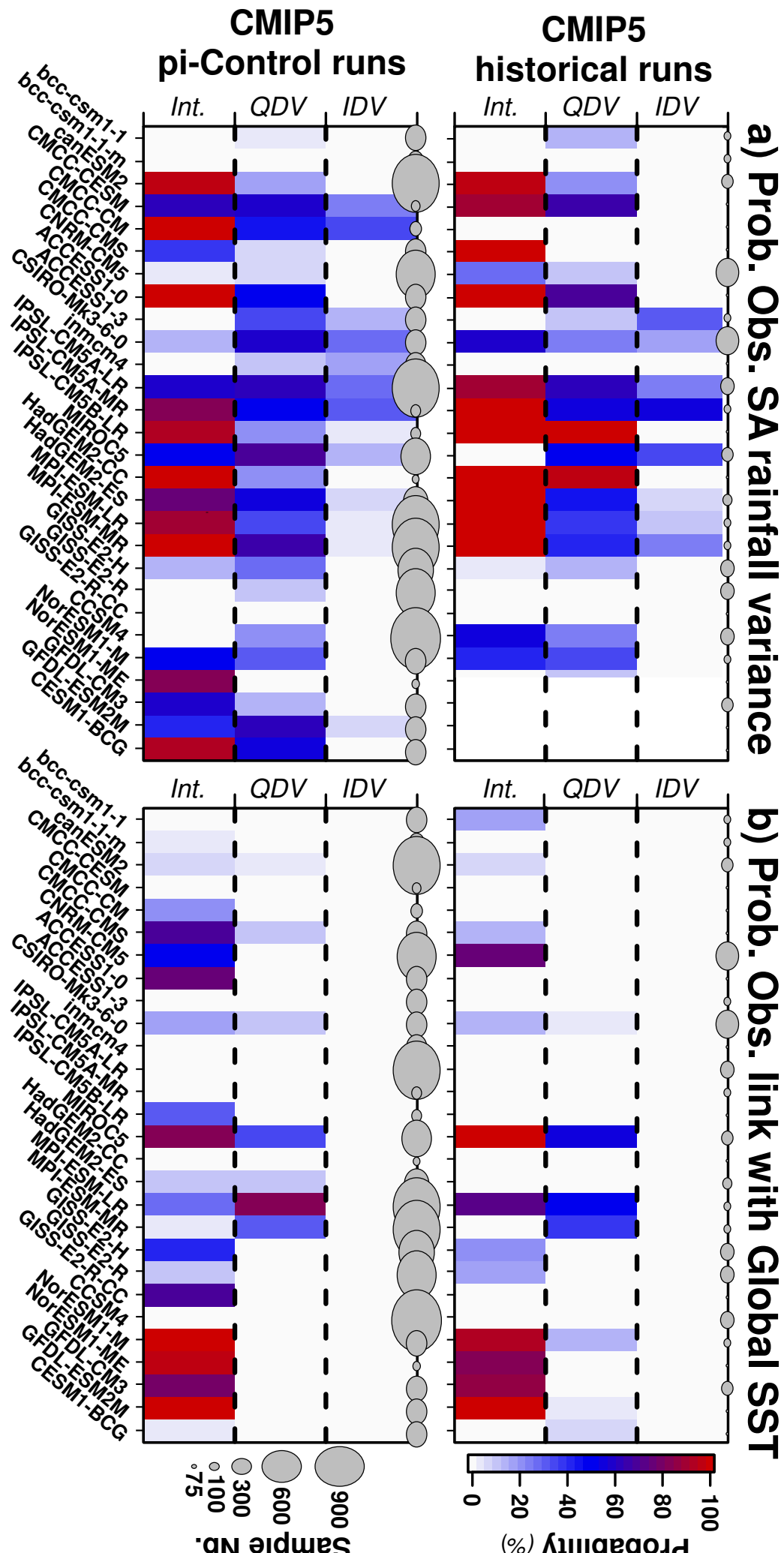


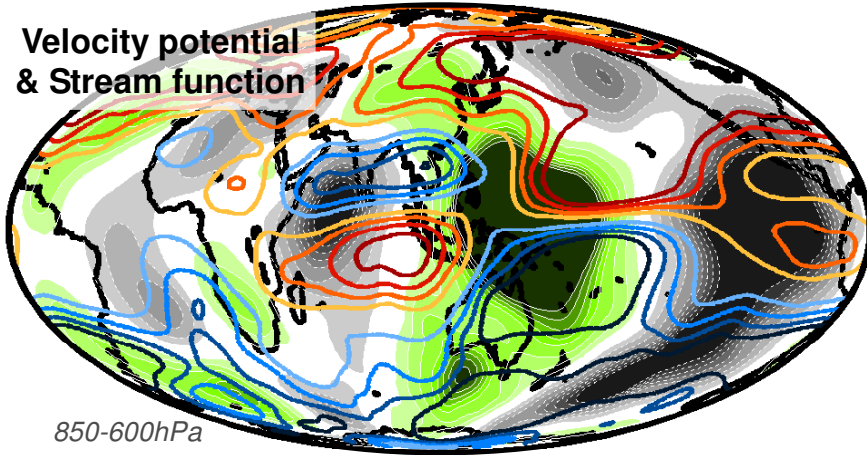
Figure 11

Lower Troposphere

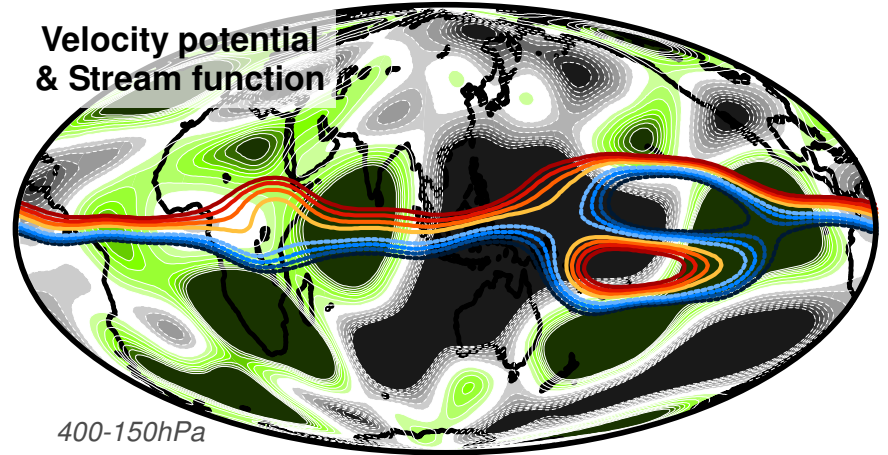
Upper Troposphere

Interannual

Velocity potential
& Stream function

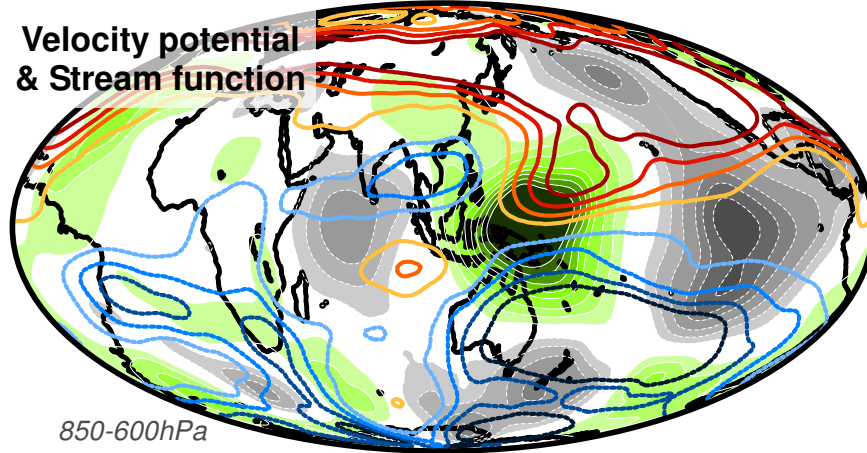


Velocity potential
& Stream function

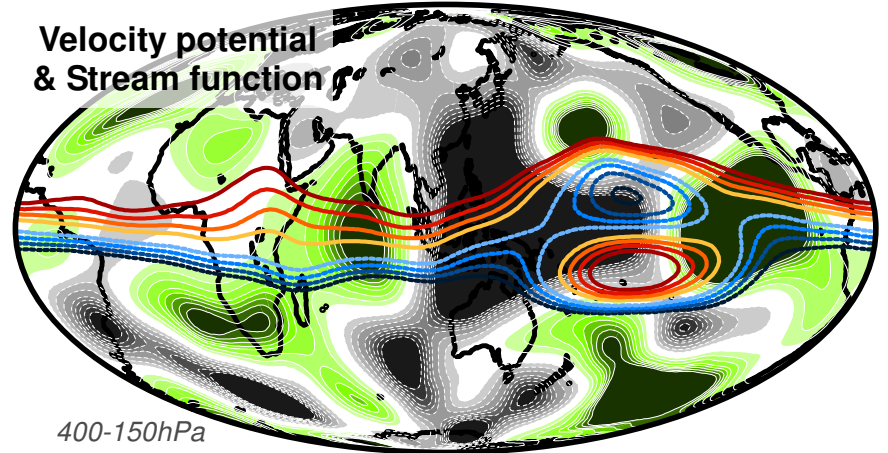


QDV

Velocity potential
& Stream function

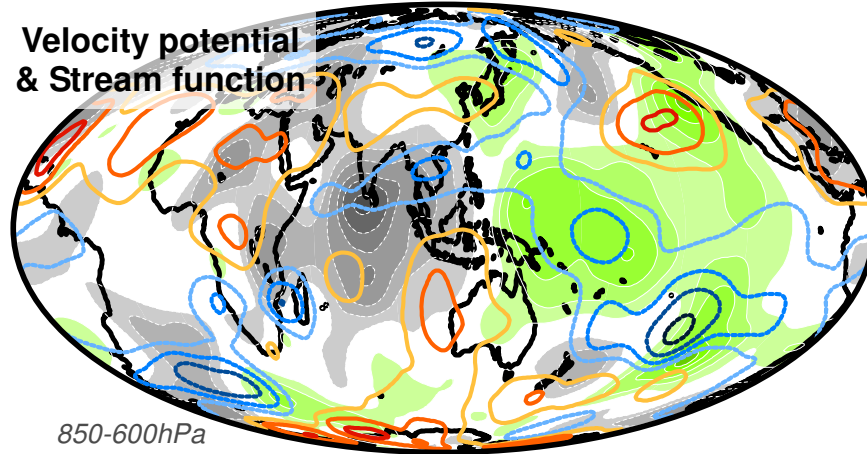


Velocity potential
& Stream function

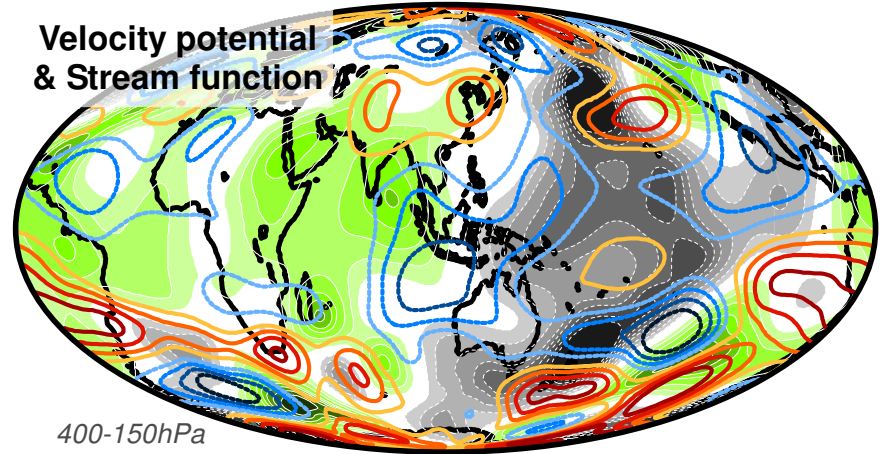


IDV

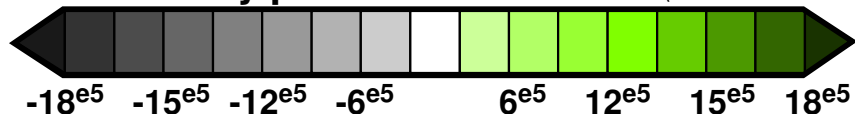
Velocity potential
& Stream function



Velocity potential
& Stream function



Velocity potential anomalies ($m^2 \cdot s^{-1}$)



Stream function anomalies ($m^2 \cdot s^{-1}$)



Figure 12

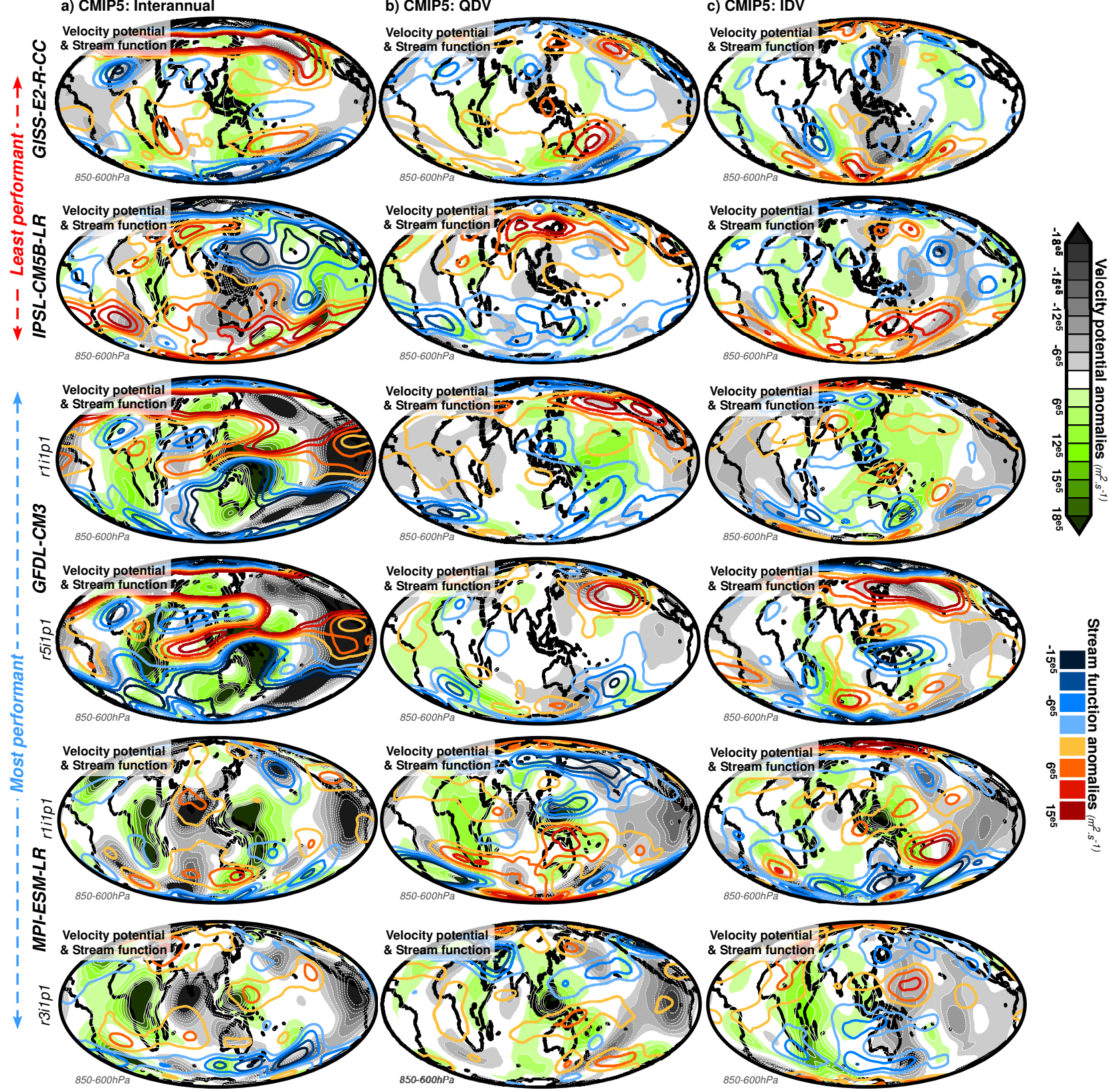






























Table 1

| Obs. | Institution | Name | Member | Variable | Hist. period | piControl length (yr) | Atmos. Grid (lat x lon) | Color ID |
|------|------------------------|---------------|--------|--------------------------|--------------|-----------------------|-------------------------|---|
| | CRU, UK | CRU TS 3.24.1 | 0 | pr | | 0 | 1 x 1 | 0 |
| | NOAA-NCDC, USA | ERSS.v4 | 0 | sst | 1901-2014 | 0 | 0 | 0 |
| | NOAA-CIRES, USA | 20CR.v2c | 56 | φ, ψ | | 0 | 2 x 2 | 0 |
| | BCC, China | bcc-csm1-1 | 3 | pr, sst, φ, ψ | 1850-2005 | 500 | 2.7906 x 2.8125 |  |
| | | bcc-csm1-1-m | 3 | | | 400 | 1.13 x 1.13 |  |
| | CCCma, Canada | CanESM2 | 5 | pr, sst, φ, ψ | 1850-2005 | 996 | 2.7906 x 2.8125 |  |
| | | CMCC-CESM | 1 | | | 277 | 3.4431 x 3.75 |  |
| | CMCC, Italy | CMCC-CM | 1 | pr, sst, φ, ψ | 1850-2005 | 329 | 0.7484 x 0.75 |  |
| | | CMCC-CMS | 1 | | | 500 | 3.7111 x 3.75 |  |
| | CNRM, France | CNRM-CM5 | 10 | pr, sst, φ, ψ | 1850-2005 | 850 | 1.4008 x 1.40625 |  |
| | CSIRO-BOM, Australia | ACCESS1-0 | 1 | pr, sst, φ, ψ | 1850-2005 | 500 | 1.25 x 1.875 |  |
| | | ACCESS1-3 | 3 | | | 500 | |  |
| | CSIRO-QCCCE, Australia | CSIRO-Mk3-6-0 | 10 | pr, sst, φ, ψ | 1850-2005 | 500 | 1.8653 x 1.875 |  |
| | INM, Russia | inmcm4 | 1 | pr, sst, φ, ψ | 1850-2005 | 500 | 1.5 x 2 |  |
| | | IPSL-CM5A-LR | 6 | | | 1000 | 1.8947 x 3.75 |  |
| | IPSL, France | IPSL-CM5A-MR | 3 | pr, sst, φ, ψ | 1850-2005 | 300 | 1.2676 x 2.5 |  |
| | | IPSL-CM5B-LR | 1 | | | 300 | 1.8947 x 3.75 |  |
| | MIROC, Japan | MIROC5 | 5 | pr, sst, φ, ψ | 1850-2005 | 670 | 1.4008 x 140625 |  |
| | | HadGEM2-CC | 1 | | | 240 | 1.25 x 1.875 |  |
| | MOHC, UK | HadGEM2-ES | 4 | pr, sst, φ, ψ | 1860-2005 | 577 | |  |
| | | MPI-ESM-LR | 3 | | | 1000 | 1.8653 x 1.875 |  |
| | MPI-M, Germany | MPI-ESM-MR | 3 | pr, sst, φ, ψ | 1850-2005 | 1000 | |  |
| | | GISS-E2-H | 6 | | | 780 | |  |
| | NASA-GISS, USA | GISS-E2-R | 6 | pr, sst, φ, ψ | 1850-2005 | 850 | 2 x 2.5 |  |
| | | GISS-E2-R-CC | 1 | | | 251 | |  |
| | | CCSM4 | 6 | pr, sst, φ, ψ | 1850-2005 | 1051 | 1.25 x 0.94 |  |
| | NCC, Norway | NorESM1-M | 3 | pr, sst, φ, ψ | 1850-2005 | 501 | 1.8947 x 2.5 |  |
| | | NorESM1-ME | 1 | | | 252 | |  |
| | | GFDL-CM3 | 5 | pr, sst, φ, ψ | 1860-2005 | 500 | 2 x 2.5 |  |
| | NOAA-GFDL, USA | GFDL-ESM2M | 1 | pr, sst, φ, ψ | 1861-2005 | 500 | 2.0225 x 2.5 |  |
| | NSF-DOE-NCAR, USA | CESM1-BCG | 1 | pr, sst, φ, ψ | 1850-2005 | 500 | 1.25 x 0.94 |  |

CMIP5 Model outputs

Table 2

| Institution | Name | Atmospheric Comp. | Ocean Comp. | Land Comp. | Sea-Ice Comp. |
|----------------------|---------------|-------------------|-------------|-------------|---------------|
| BCC, China | bcc-csm1-1-1 | BCC-AGCM2-1 | MOM4-1 | BCC-AVIM1-0 | SIS |
| | bcc-csm1-1-m | BCC-AGCM2-1 | | | |
| CCCma, Canada | CanESM2 | CanCM4 | CanOM4 | CTEM | o |
| | CMCC-CESM | | | | |
| CMCC, Italy | CMCC-CM | ECHAM5 | OPA8-2 | SILVA | LIM |
| | CMCC-CMS | | | | |
| CNRM, France | CNRM-CM5 | ARPEGE | NEMO3-2 | ISBA | GELATO |
| | ACCESS1-0 | HadCM3 | | | |
| CSIRO-BOM, Australia | ACCESS1-3 | MO GA1-0 | MOM4-1 | MOSES2 | CICE |
| | CSIRO-Mk3-6-0 | CSIRO-Mk3 | MOM2-2 | o | ~CICE |
| INM, Russia | inmcm4 | INMAM | INMOM | o | o |
| | IPSL-CM5A-LR | LMDZ5A | NEMO3-2 | ORCHIDEE | LIM |
| IPSL, France | IPSL-CM5A-MR | | | | |
| | IPSL-CM5B-LR | LMDZ5B | | | |
| MIROC, Japan | MIROC5 | FRCGCM | COCO | MATSIRO | COCO |
| | HadGEM2-CC | HadCM3 | HadGOM1 | MOSES2 | CICE |
| MOHC, UK | HadGEM2-ES | | | | |
| | MPI-ESM-LR | ECHAM6 | MPI-OM | JSBACH | o |
| MPI-M, Germany | MPI-ESM-MR | | | | |
| | GISS-E2-H | | Russel | | |
| NASA-GISS, USA | GISS-E2-R | ModeIE2 | HYCOM | o | o |
| | GISS-E2-R-CC | | | | |
| NCAR, USA | CCSM4 | CAM4 | POP | CLM4 | CICE |
| | NorESM1-M | CAM4 | MICOM | CLM4 | CICE |
| NCC, Norway | NorESM1-ME | | | | |
| | GFDL-CM3 | AM3 | MOM4-1 | LM3 | SIS |
| NOAA-GFDL, USA | GFDL-ESM2M | AM2 | | | |
| | CESM1-BCG | CAM4 | POP2 | CLM4 | CICE |

CMIP5 Model outputs